electricity

MDPI

Article

Average Modeling of High Frequency AC Link Three-Port DC/DC/DC Converters

Eduardo Vasquez Mayen * and Emmanuel De Jaeger

Mechatronic, Electrical Energy, and Dynamic Systems, Université Catholique de Louvain (UCLouvain), 1348 Louvain-la-Neuve, Belgium; emmanuel.dejaeger@uclouvain.be

* Correspondence: eduardo.vasquez@uclouvain.be

Abstract: The current transition towards renewable energies has led to an increased utilization of Photovoltaic (PV) sources and battery energy storage systems to complement the PV panels. To facilitate energy transfer among PVs, batteries, and loads, multiple converters are required. Thus, this transformation in the energy system has resulted in an increase in converter-interfaced elements. Within this context, three-port converters allow for replacing multiple converters with a single one. These three-port converters use a high-frequency AC resonant link for the bidirectional transfer of energy across the different ports. This architecture uses multiple switches and has a variable operating frequency. These characteristics make the simulation of these converters computationally heavy. Thus, averaged models are required, especially for simulating multiple converters connected in parallel or composing a microgrid. In this paper, an averaged model for this type of converter is developed. The methodology is first demonstrated and applied to a two-port DC/DC converter, and subsequently extended to the three-port DC/DC/DC version. Afterwards, control strategies for three-port DC/DC/DC converters are proposed based on the elements connected to their ports. The developed model for three-port DC/DC/DC converters is then implemented in an islanded DC microgrid to demonstrate their parallel operation. The proposed developed averaged models and the test DC microgrid are implemented in MATLAB/Simulink.

Keywords: high-frequency AC link; DC microgrid; three-port converters

check for updates

Citation: Vasquez Mayen, E.; De Jaeger, E. Average Modeling of High Frequency AC Link Three-Port DC/DC/DC Converters. *Electricity* **2024**, *5*, 397–425. https://doi.org/10.3390/electricity5020021

Academic Editors: Pedro S. Moura and Ana Soares

Received: 20 March 2024
Revised: 15 May 2024
Accepted: 11 June 2024
Published: 17 June 2024

Copyright: © 2024 by the authors. Licensee MDPI, Basel, Switzerland. This article is an open access article distributed under the terms and conditions of the Creative Commons Attribution (CC BY) license (https://creativecommons.org/licenses/by/4.0/).

1. Introduction

The adoption of renewable energies has increased in recent years. Among these energies, Photovoltaic (PV) energy has become one of the most widely used. The widespread adoption of PVs has also led to the integration of energy storage devices, such as batteries. By coupling a battery with a PV system, the intermittent nature of PV energy can be addressed, enabling the storage of surplus energy for complementary usage and power regulation. Both the PVs and the batteries are connected via DC/DC or DC/AC converters. However, the disadvantage of such a system is that the use of multiple converters can lead to reduced efficiency, increased size, and possibly higher costs [1]. This trend is expected to persist as renewable energy penetration rises and new loads, such as Electric Vehicles (EVs), are added to the energy distribution system. In order to maximize the efficiency of such a system, research on the converters interfacing with the different elements has been conducted.

In this context, three-port converters have potential applications. These converters enable the connection of multiple elements using a single converter, thus reducing the number of converters needed. The three-port converter analyzed in this paper is a soft-switched High-Frequency AC (HFAC) link converter. This converter can be seen as an extension of a buck-boost converter where a capacitor is placed in parallel with the link inductor. The LC circuit creates resonating transients that allow for Zero Voltage Switching (ZVS). This type of converter can be classified as a Quasi-Square Wave (QSW) converter [2]. The use of an HFAC link provides several advantages [3,4]:

- It allows to change the link voltage for each converter port.
- It provides electrical isolation between the converter ports.
- It has an inherent bi-directional power flow capability.
- It provides a reduction in the size and weight of heat dissipating components.

The parallel HFAC link architecture was initially introduced as a universal power converter in [5]. The authors of [6] proposed a soft-switching AC link converter for medium- and high-power applications, overcoming previous drawbacks such as the inability to supply output current at low voltages and a large dead time. This work was further explored in [7], showcasing the proposed converter as an AC/AC or AC/DC buck-boost converter for medium-voltage applications. In [8,9], the capabilities of the HFAC link converter as a PV inverter were showcased, highlighting its negligible converter losses due to the ZVS and the compactness of its high-frequency link inductor. The work in [10] connects several PV strings with different voltage levels via the use of this converter. In [11], the capabilities of the ZVS HFAC link inverter as a multiport system were demonstrated. The application of this converter for AC microgrids is explored in [12], where it is proposed that the application of the converter can be expanded to more than three ports. This three-port converter architecture has also been proposed as a technical solution for efficient delivery of energy to electric vehicle charging terminals in [13]. The work in [13] illustrated the converter's versatility, highlighting its capability to function as an AC/DC/DC converter or as a DC-only converter.

Detailed studies have been performed on the switching mechanisms of the topology, as well as the computation of the different commutation periods [14,15]. However, to the best of the authors' knowledge, a research gap exists regarding the average modeling of this particular converter type. Indeed, detailed modeling of the switching mechanisms of this architecture can be computationally intensive. This complexity poses challenges when simulating distribution systems or microgrids that involve the parallel connection of multiple of these converters. Thus, there is a need to develop averaged models that preserve the system's defining characteristics while alleviating computational complexity. The following paper aims to provide an average model based on the state-space modeling of this converter architecture. The proposed method provides an averaged model that allows for retaining the main characteristics of the converter while reducing computational complexity.

To develop and validate the average model, three different types of models are dealt with. The most complex model is the switched model, which implements the converter with the corresponding switching dynamics. This type of model provides the most detail at the cost of high computational demand. The next type of model dealt with is the state-space model. The state-space model develops an equivalent linearized model to which certain simplifications can be applied. The main difference between the switched and state-space models is that the state-space model provides the average values, neglecting the switching dynamics. From the state-space model, the transfer functions for the state variables can be obtained. These transfer functions are obtained using the state-space model along with the state-transition matrix and are an equivalent single-input–single-output representation of the state-space system. The final model studied is the proposed average model, utilizing the DC transformer representation. This model provides average values the same as the state-space model; however, it has two main differences. First, it allows translating the state-space model into a circuit representation that can be interfaced with different elements. Secondly, the control signal for the converter can be easily modified during simulation. This allows the implementation of different control loops.

To this end, this paper presents the following sections. Section 2 develops the proposed model for a two-port converter. A two-port converter is presented initially to allow the reader to better understand the converter architecture. Section 2 first illustrates the operation of the converter and the HFAC link. Afterwards, the state-space model for the converter is developed. The state-space model is then validated by comparing its output to the expected results from the converter analytical equations. Finally, the average model is presented and implemented in Matlab/Simulink. The proposed average model is validated by comparing its output to the converter switch model. Section 3 presents the modeling for three-port DC/DC/DC

converters. Two cases are studied: a converter with two sources and one load, and a converter with one source and two loads. Here, the state-space model for both cases is developed, and the consequent average model is presented. Section 4 briefly presents the proposed control methods for the three-port converters according to the elements connected to each port. These elements include PVs with Maximum Power Point Tracking (MPPT), batteries, loads, and the implementation of droop control for DC microgrid connection. Section 5 shows the implementation of the developed three-port converters and their control schemes in a small test DC microgrid. Finally, the conclusions and future work are given in Section 6.

2. Modeling of Two-Port DC/DC Converters

First, the modeling of a two-port converter is developed. This allows us to study and explain the functioning of the converter and the proposed modeling in a simple case. The schematic of the studied two-port HFAC link converter is shown in Figure 1. The converter has two DC ports and the HFAC link composed of an inductor and a capacitor. Notice that the switches connecting the ports to the HFAC link are bidirectional switches. Thus, through the proper switching technique, both DC ports have bidirectional power flow.

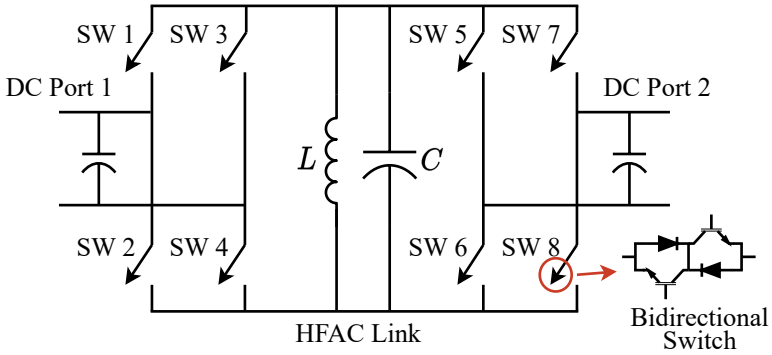


Figure 1. Schematic of a two-port DC-DC HFAC link converter.

2.1. Converter Operating Principle

The operational principle of the converter is detailed hereafter, as in [15]. The case where a source is connected to DC Port 1 and feeds a load connected to DC Port 2 is considered.

Mode 1: Link Charge When the HFAC link reaches a voltage equal to that of DC Port 1, the HFAC link is connected to the port through switches SW1 and SW4. This condition is necessary to ensure ZVS. Once the connection is made, current is transferred from DC Port 1 to the HFAC link, as shown in Figure 2. This current charges the inductance of the HFAC link, which stores this energy. The current present in the HFAC link can be calculated via Equation (1), which is based on the inductor voltage equation. The charging will continue until a reference current value for the inductance is reached. After the reference value is attained, the HFAC link disconnects from DC Port 1, and Mode 2 is started. Notice that, due to the fast dynamics of the HFAC link, the voltage of DC port 1 can be regarded as constant.

$$i_{Link} = \frac{1}{L}\int_0^t V\,dt = \frac{V(t)}{L} + i_{Link}(0) \tag{1}$$

Mode 2 and 4: Partial Resonance After Mode 1, the HFAC link enters the partial resonance mode. During this mode, the HFAC link does not connect to a port and remains isolated, as shown in Figure 3. Because the HFAC link is composed of an inductor in parallel with a capacitor, a resonance will occur. During this resonance, energy will be exchanged between the elements of the HFAC link. This exchange of energy results in a change in the HFAC link voltage. The purpose of this mode is to allow the HFAC link voltage to evolve until it becomes equal to the voltage of the next port. This condition is once again respected in order to ensure ZVS. During the resonance, the voltage of the inductor and the current of the capacitor can be described through Equations (2) and (3).

$$i_C = -i_{Link} = C\frac{dV_{Link}}{dt} \tag{2}$$

$$V_{Link} = L\frac{di_{Link}}{dt} \tag{3}$$

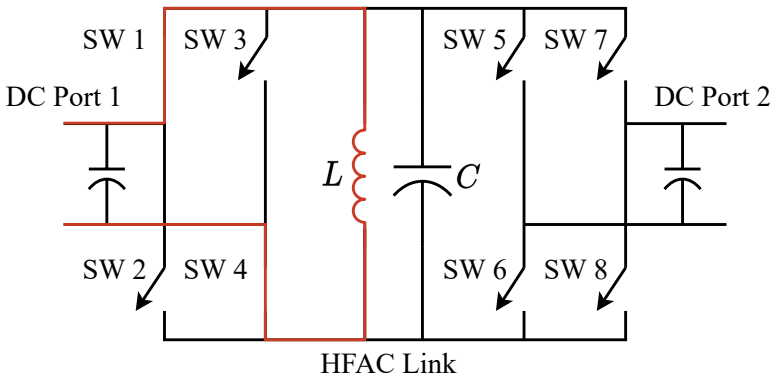


Figure 2. Two-port DC/DC converter circuit diagram during Mode 1 ©2023 IEEE. Reproduced with copyright permission from [15].

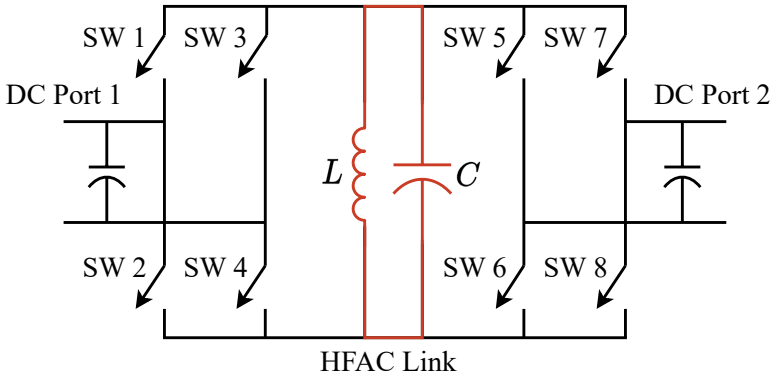


Figure 3. Two-port DC/DC converter circuit diagram during Modes 2 and 4 ©2023 IEEE. Reproduced with copyright permission from [15].

Mode 3: Link Discharge After the partial resonance mode, the voltage of the HFAC link becomes equal to that of DC Port 2. This allows the HFAC link to connect to DC Port 2 with ZVS. As shown in Figure 4, this connection is performed with inverse polarity via SW5 and SW8. This inverse polarity allows the HFAC link to discharge the current stored in its inductance and supply the load. The discharge continues until a set minimum current remains in the HFAC link. Once this minimum current is reached, the HFAC link disconnects from DC Port 2. This small amount of current is left in the HFAC link to facilitate its next resonance stage, Mode 4.

As previously described, Mode 4 is a partial resonance stage similar to Mode 2. The HFAC link will once again isolate itself in order to cause a resonance. Thanks to the set minimum current left in the HFAC link, the parallel circuit can resonate and adjust its voltage level back to that of DC Port 1. This will allow it to reconnect to DC Port 1 and start another charge and discharge cycle.

The converter operating principle is summarized in Figure 5. First, the HFAC link is connected to the input port. The inductance of the link is charged with a voltage, V_{in}. Due to a constant voltage being applied to the inductance, the current increases linearly. Once it has been charged to the desired level, the HFAC link is disconnected and resonance occurs due to the parallel LC circuit. Through this resonance, the voltage level is changed. Once the voltage level of the output port, V_{C_f}, is reached, the HFAC link is connected with opposite

polarity, and the inductance then discharges to the load. Since a constant output voltage is applied, the current is also discharged linearly. Once discharged, another resonance that goes through a maximum voltage level, V_{max}, occurs. This resonance changes the voltage back to the input voltage level. This is done with opposite polarity to transfer energy more efficiently.

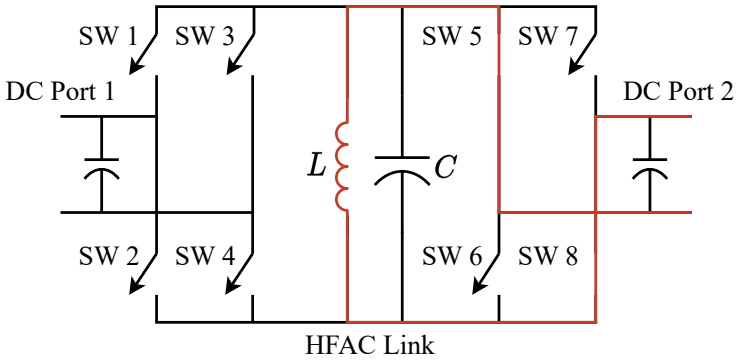


Figure 4. Two-port DC/DC converter circuit diagram during Mode 3 ©2023 IEEE. Reproduced with copyright permission from [15].

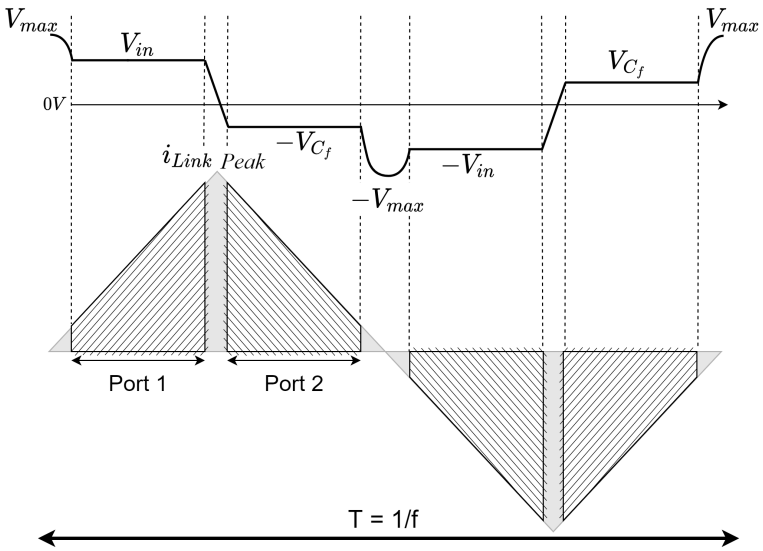


Figure 5. Two-port DC/DC converter HFAC link voltage and current waveform.

The losses in this type of converter have been addressed briefly in the literature. In terms of turn-on, this converters uses ZVS. Thus, during the resonance mode the HFAC link voltage is adjusted until it matches that of the port it will connect to, resulting in equal voltage for the port and the HFAC link, producing ZVS. During switch turn-off, the link capacitance acts as a buffer, resulting in low turn-off losses [6]. The work in [7] highlights the main losses in this type of converter. These losses are mainly attributed to conduction losses that depend on the switch voltage and resistance, parasitic inductance losses, turn-off losses, and link-inductance losses.

2.2. State-Space Model

The simplified averaged model is developed using the state-space equations of the circuit shown in Figure 6. In this state-space model, two major simplifications are considered. First, the resonance periods are not considered. The reason for this is that no energy transfer is performed during these periods; thus, for an averaged model their impact is negligible. Additionally, the work in [15] showed that, under normal operation, these resonance periods have a negligible duration with respect to the total period. Furthermore, to consider them, extra duty cycles are required. This, in turn, makes the control of the

average model more complex. The second simplification is that the capacitance of the HFAC link is neglected. The reason for this is that the capacitance only participates in the resonance periods but does not participate in the storage or transfer of energy itself. Thus, it can be neglected without affecting the general results of the averaged model. However, the HFAC link capacitor is still illustrated in Figure 6 to help identify the HFAC link.

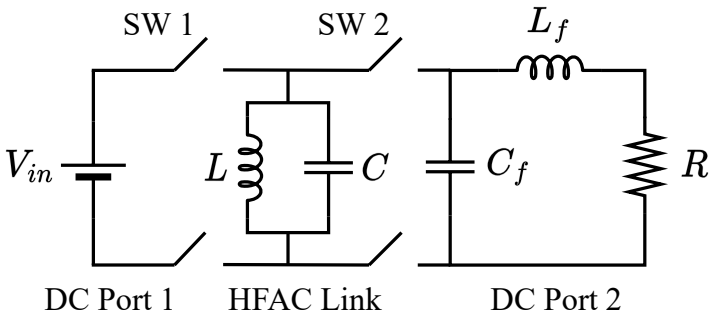


Figure 6. Two-port DC/DC converter simplified circuit diagram.

With the previous simplifications applied, the state variables considered are the link-inductance current, I_L, the output filter capacitance voltage, V_{C_f}, and the output filter inductance current, I_{L_f}. The voltage, V_{in}, is considered as the only input. When switch SW1 is closed, the system is defined by the equations shown in (4). The inductance is charged by the input voltage, while the output capacitance discharges towards the load, R. Note that the output current is $C_f\, dV_{C_f}/dt = -V_{C_f}/R$ when the impact of the filter inductance L_f is negligible; otherwise, it is $C_f\, dV_{C_f}/dt = -I_{L_f}$. The second state is when SW2 is closed, and thus the inductance discharges itself toward the load. This final state is described by the equations shown in (5).

$$\begin{cases} L\frac{dI_L}{dt} = V_{in} \\ L_f\frac{dI_{L_f}}{dt} = -I_{L_f}R + V_{C_f} \\ C_f\frac{dV_{C_f}}{dt} = -\frac{V_{C_f}}{R} \end{cases} \tag{4}$$

$$\begin{cases} L\frac{dI_L}{dt} = V_{C_f} \\ L_f\frac{dI_{L_f}}{dt} = -I_{L_f}R + V_{C_f} \\ C_f\frac{dV_{C_f}}{dt} = -I_L - \frac{V_{C_f}}{R} \end{cases} \tag{5}$$

With the previous equations in hand, the state-space model can be defined through a state matrix, A, input matrix, B, and the state vector, x. The duration of the periods where SW1 or SW2 is closed is represented by the duty cycles d_1 and d_2, respectively. Thus, the state-space model can be formulated as:

$$\dot{\bar{x}} = A\bar{x} + B\bar{u}, \tag{6}$$

where:

$$A = d_1A_1 + d_2A_2$$
$$B = d_1B_1 + d_2B_2$$
$$A_1 = \begin{bmatrix} 0 & 0 & 0 \\ 0 & \frac{-R}{L_f} & \frac{1}{L_f} \\ 0 & 0 & -\frac{1}{C_f R} \end{bmatrix}, A_2 = \begin{bmatrix} 0 & 0 & \frac{1}{L} \\ 0 & \frac{-R}{L_f} & \frac{1}{L_f} \\ -\frac{1}{C_f} & 0 & -\frac{1}{C_f R} \end{bmatrix}$$
$$B_1 = \begin{bmatrix} \frac{1}{L} \\ 0 \\ 0 \end{bmatrix}, B_2 = \begin{bmatrix} 0 \\ 0 \\ 0 \end{bmatrix}, \bar{x} = \begin{bmatrix} I_L \\ I_{L_f} \\ V_{C_f} \end{bmatrix}$$

From the state-space system, the definition for the steady-state values of the state variables is found as:

$$\begin{cases} I_L = \frac{V_{in}\, d_1}{R\, d_2^2} \\ I_{L_f} = -\frac{-V_{in}\, d_1}{R\, d_2} \\ V_{C_f} = \frac{-V_{in}\, d_1}{d_2} \end{cases}. \tag{7}$$

Furthermore, using the state-transition matrix $\Phi = (sI - A)^{-1}$, the following transfer functions can be obtained through $H(s) = C\Phi B + D$:

$$\begin{aligned} \frac{I_L}{V_{in}} &= \frac{d_1(1 + C_f R s)}{C_f L R s^2 + L s + R d_2^2} \\ \frac{I_{L_f}}{V_{in}} &= \frac{-R d_1 d_2}{(R + L_f s)\,(C_f L R s^2 + L s + R d_2^2)} \\ \frac{V_{C_f}}{V_{in}} &= \frac{-R d_1 d_2}{C_f L R s^2 + L s + R d_2^2} \end{aligned}. \tag{8}$$

2.3. Model Validation

To validate the model found, the output of the state-space model will be compared to the steady-state values calculated through the equations of the detailed model. Namely, it will be verified that, with the same inputs, the state-space model outputs the correct average inductor current, I_L, output current, I_{L_f}, and output voltage, V_{C_f}. From the procedure shown in [14], the inductance, L, can be sized based on the maximum power and a chosen link frequency. For this example, a converter with the parameters summarized in Table 1 is considered.

Table 1. Two-port DC/DC converter parameters.

Parameter	Value
P_{max} (kW)	20
Link Frequency (kHz)	5
V_{in} (V)	750
V_{C_f} (V)	375
Link inductance (mH)	0.156
Filter inductance (µH)	6.2
Filter capacitance (mF)	120

To test the model, first, a load of 12 kW is tested. Based on the power and the port voltages, I_{Lpeak} is calculated as shown in (9) [9,12]. Using the relationship between voltage and current in an inductor, the charge, t_1, and discharge, t_2, periods are found. Once the charge and discharge periods are found, the period can be calculated as shown in Equation (12). Once the total period is known, the duty cycle for each port can be calculated using Equation (13). To calculate the average current, the integral of the current waveform is taken. As shown in Figure 5, the currents have a triangular waveform. Thus, the integral of the waveforms can be calculated as the areas of the triangles. The average input current and output current are the areas of their corresponding triangles over a period, T. The average current of the link inductance, L, can also be calculated using the whole waveform using Equation (14).

The values from Table 1 are used with the previously described equations to compute the inductor current, I_L, output current, I_{L_f}, and output capacitor voltage, V_{C_f}. These same parameters are used in the state-space model described in Equation (6), considering a duty cycle of $d_1 = 0.3333$ and $d_2 = 0.6667$, calculated using Equation (13). The system of equations is then solved for x, yielding the steady-state values for the state variables. Table 2 compares the values obtained using the analytical equations with those from the state-space model. The results show that both methods provide identical values, therefore

validating the state-space model. The given output voltage corresponds to the desired output. Furthermore, the output current, I_f, corresponds to the desired output power of 12 kW. The average current, I_L, also provides the expected result when compared against Equation (14).

$$I_{Lpeak} = 2\sqrt{P}\left(\frac{\sqrt{P}}{V_{in}} + \frac{\sqrt{P}}{V_{C_f}}\right) \tag{9}$$

$$t_1 = \frac{I_{Lpeak}\, L}{V_{in}} \tag{10}$$

$$t_2 = \frac{I_{Lpeak}\, L}{V_{C_f}} \tag{11}$$

$$T = t_1 + t_2 \tag{12}$$

$$d_1 = \frac{t_1}{T};\; d_2 = \frac{t_2}{T} \tag{13}$$

$$I_{Lavg} = \frac{1}{T}\left(0.5\, t_1\, I_{Lpeak} + 0.5\, t_2\, I_{Lpeak}\right) \tag{14}$$

Table 2. Two-port DC/DC converter state-space model output values comparison.

Parameter	Analytical Equations	State-Space Model
I_L (A)	48	48
I_{L_f} (A)	−32	−32
V_{C_f} (V)	−375	−375

The step response of the voltage, V_{C_f}, to the input, V_{in}, is shown to give the correct value in the step response of Figure 7. Additionally, the impact that each parameter has on the response of the system's output voltage, V_{C_f}, is shown in Figure 8 through a pole-zero plot. In Figure 8, only one parameter was modified at a time. The inductance and capacitance values were increased by steps of 50 µH and 50 µF, respectively. The resistance parameter was increased in steps of 5 Ω. It can be observed that the inductance, L, only affects the frequency of the oscillations in the system. Meanwhile, the load resistance, R, only influences the damping. Finally, the filter capacitance, C_f, affects both the damping and the frequency. Furthermore, all of the poles are located in the left-hand plane, indicating that the system is stable.

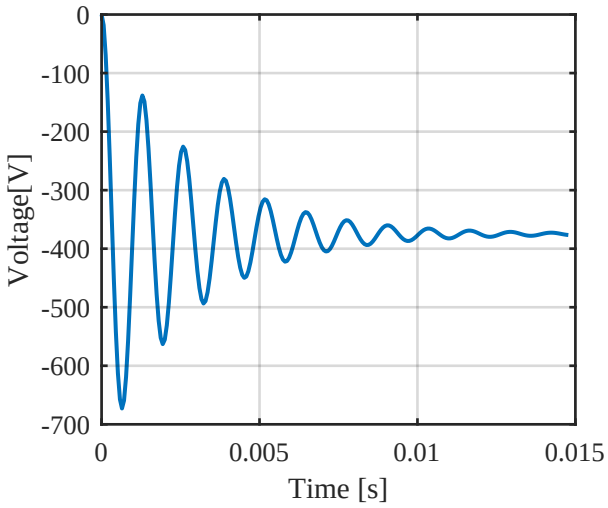


Figure 7. Two-port DC/DC converter state-space output voltage, V_{C_f}, step response to input V_{in}.

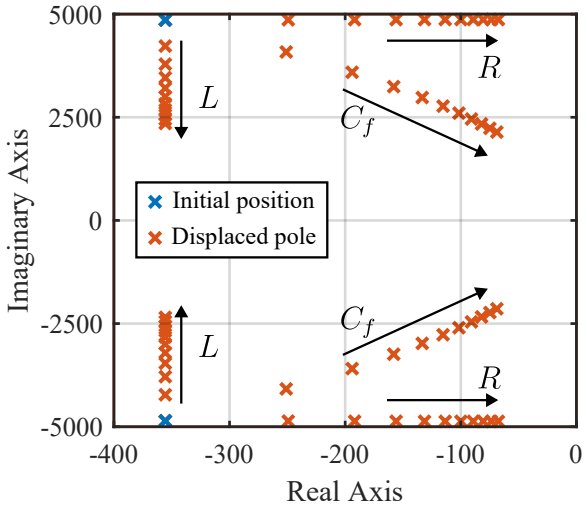


Figure 8. Influence of components parameters on two-port DC/DC converter state-space output voltage, V_{C_f}, response.

2.4. Average Model

The primary aim of the developed model is to provide an averaged model that can be effectively utilized in dynamic simulations without imposing a significant computational burden. To this end, the concept of a DC transformer is used. The average model using the DC transformer is a circuit realization of the state-space model that allows representing the relationships between the voltages and currents of the converter [16,17]. The DC transformer operates as an ideal transformer with a conversion ratio that is a function of the duty cycle. The main advantage of this method is that the voltage, current, and duty-cycle values are retained, while the switching is neglected. Because the switching behavior does not need to be modeled, the computational burden is significantly reduced. The implementation of the DC transformer is performed through the use of the Variable-ratio transformer block [18] in MATLAB/Simulink R2022a.

The two-port converter is implemented as shown in Figure 9, with the parameters of Table 1. The proposed configuration allows controlling the system via the duty cycles while being able to measure the current of the link inductance placed between the two Variable-ratio transformers. Notice that when $d_1 = 1$ and thus $d_2 = 0$, the circuit corresponds to the simplified circuit of Figure 6 with SW1 closed and SW2 open. Meanwhile, when $d_1 = 0$ and $d_2 = 1$, the circuit corresponds to the simplified circuit with SW1 open and SW2 closed. The output filter and the load are connected with inverted polarity, but the system can provide the same results with a positive sign if connected with normal polarity.

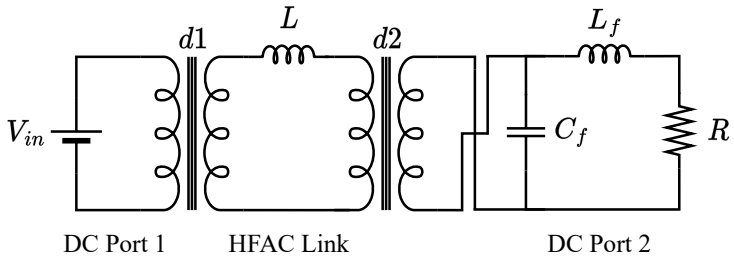


Figure 9. Two-port DC/DC average converter implementation.

Three different signals are shown as results. First, the output voltage is shown in Figure 10a, where it is seen that, after the initial response, the system reaches the desired output voltage value of -375 V. Furthermore, it is seen that the initial response exhibits a consistent alignment with the step response that was shown in Figure 7. Afterwards, in Figure 10b,c the resulting currents in the link and the output port are shown respectively.

The link current, I_L, is shown to converge to the expected value of 48 A, as described previously. Equally, the output current has a final value of -32 A, which results in the desired power transfer of 12 kW.

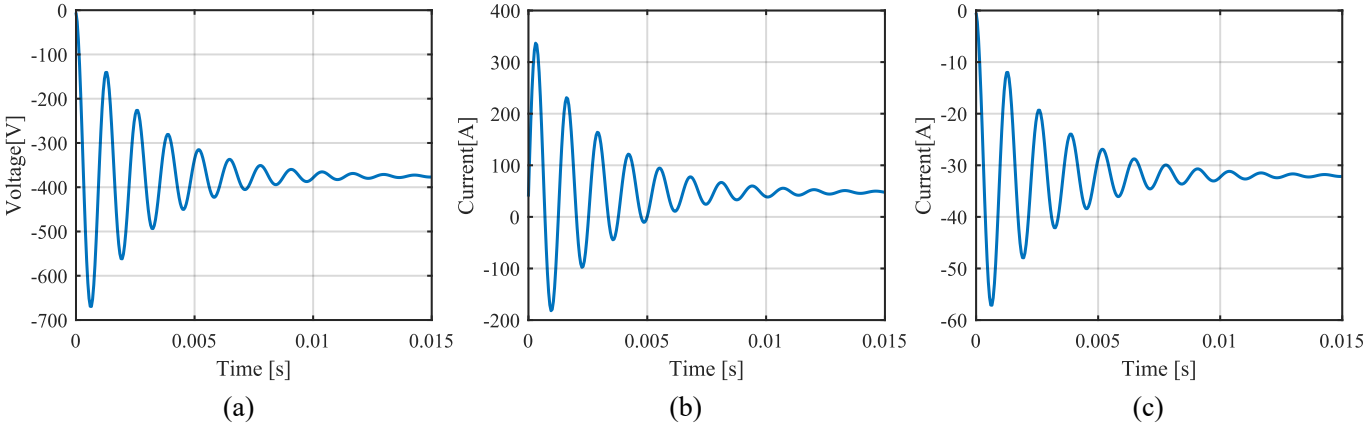


Figure 10. Two-port DC/DC converter average model output: (**a**) Output voltage, V_{C_f}, (**b**) Link current, I_L, (**c**) Output inductance current, I_{L_f}.

To further validate the model, the response of the output voltage to a drop in input voltage is investigated. The response is compared to that of the transfer function. The system is stable, with an output voltage of -375 V when at time $t = 0.5$ s; a 5% voltage drop occurs on the input voltage. The response of the dynamic model and the transfer function are compared in Figure 11. The result shows that the systems have the same response and stabilize to the same output voltage of -356.25 V. Thus, it is shown that the proposed model captures the dynamics of the converter.

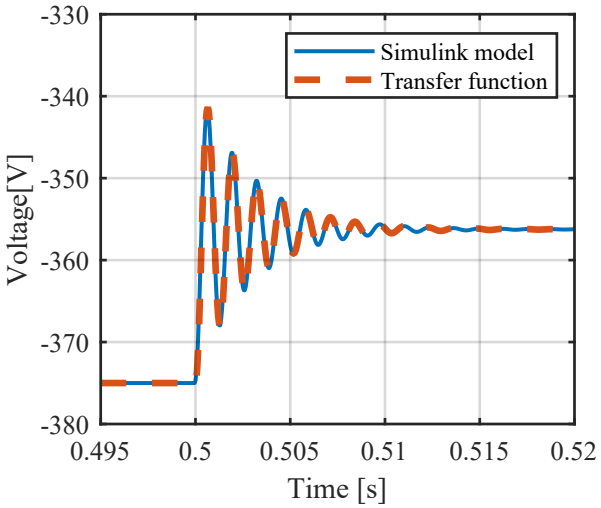


Figure 11. Two-port DC/DC converter output voltage response to a 5% input voltage drop.

As a final validation step, the proposed average model is compared against the switched model of the converter. A two-port HFAC link converter has been implemented in Matlab/Simulink, as shown in Figure 12. This switched model is not controlled via the duty cycle. Instead, the switching is performed based on a reference peak HFAC link current, I_{Lpeak}, and the measured HFAC link voltage and current.

The parameters used are the same as for the average model. The bidirectional switches are implemented with MOSFET switches. The parasitic elements of the inductors and capacitors are not considered in the simulated circuit. The switches are implemented with an on resistance of $R_{on} = 1$ μΩ and a diode forward voltage of $V_d = 0.1$ V. Figure 13 shows

the resulting currents of the switched model. Specifically, the current of the HFAC link and the current of the switches are shown. Only SW1, SW3, SW6, and SW8 are shown, as the other switches act complementarily. It is observed that the HFAC link follows the waveform described in the operating principle. Similarly, the port charge and discharge can be easily seen through the switch currents. Whenever the switches conduct, the triangular waveform is apparent. Otherwise, when they do not conduct, the current is zero. Notice that the resonance periods can be observed at the moments where no switch is conducting.

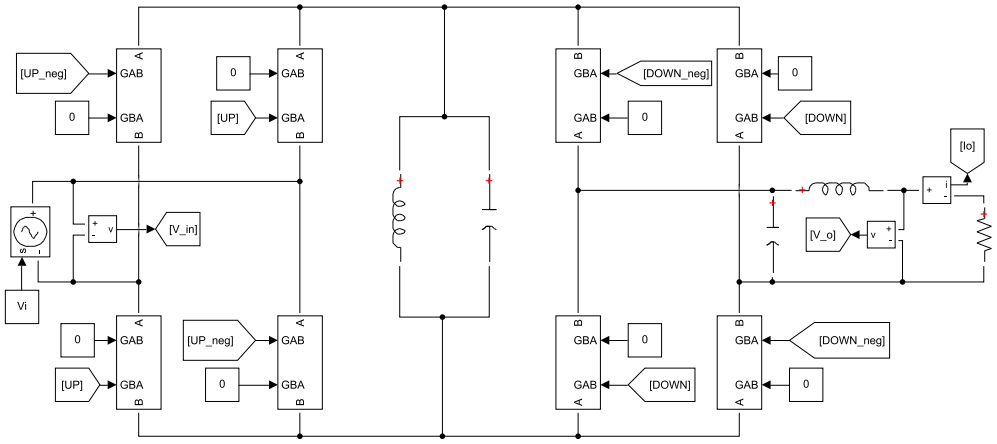


Figure 12. Two-port DC/DC converter switch model Simulink implementation.

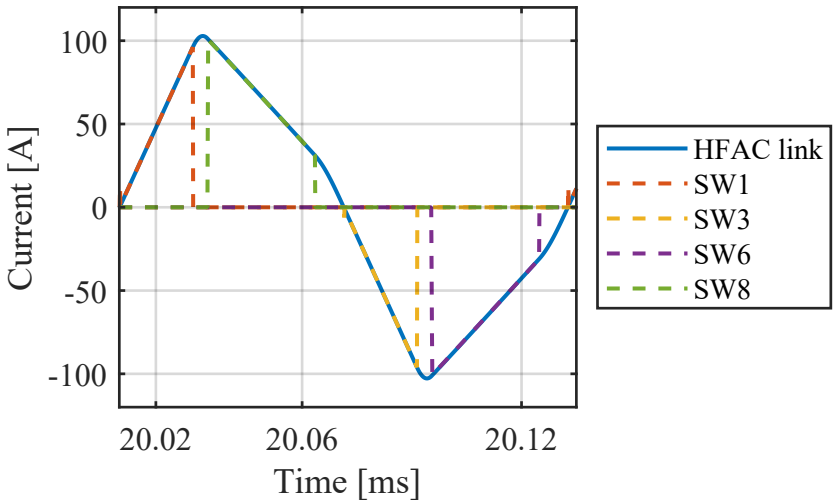


Figure 13. Two-port DC/DC converter switches model HFAC link and switch currents.

Using the same parameters as before, both models are given the corresponding references to provide an output voltage, V_{C_f}, of 375 V. At $t = 25$ ms, the reference is changed so that the output voltage becomes 350 V. Specifically, the switched model first has a reference $I_{Lpeak} = 96$ A, which then becomes $I_{Lpeak} = 87.6089$ A. The averaged model has a reference $d_1 = 0.3333$, which then changes to $d_1 = 0.3182$. The obtained results for the output voltage and HFAC link current are shown in Figure 14a,b, respectively. The results show that the average model follows the switch model correctly. A small difference can be observed in the steady-state value, which can be attributed to the average model being ideal. For example, the diode resistance and forward voltage are not considered. It is observed that the transient dynamic of the average model oscillates before reaching its steady-state value. This is due to the step caused by the change in reference. If a control is implemented that changes the reference gradually, the oscillatory response will be attenuated. This is shown in Figure 15, where instead of a step, a ramp signal is used to gradually increase the reference value.

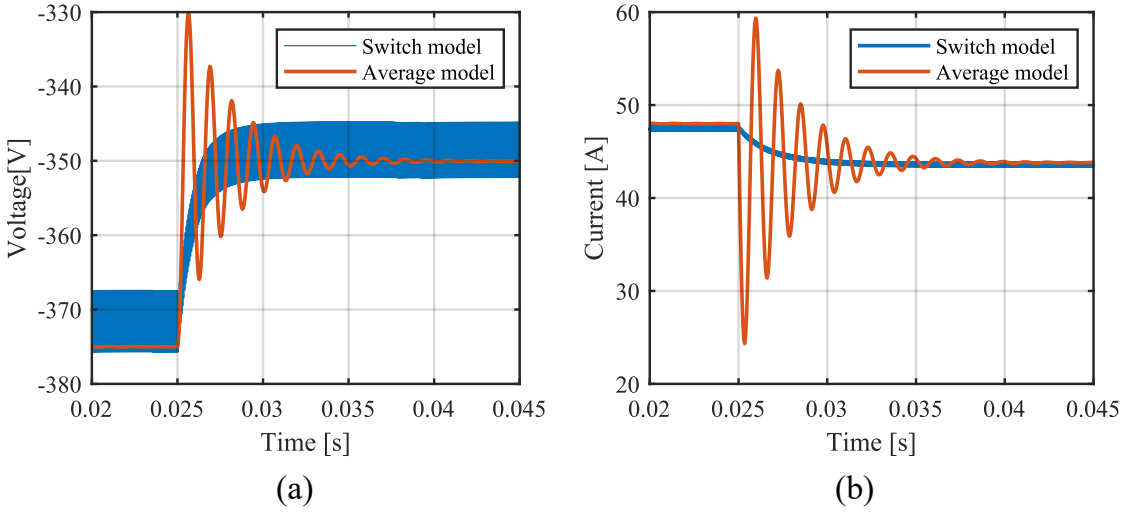


Figure 14. Switch and average two-port DC/DC converter step response comparison: (**a**) Output voltage, (**b**) HFAC link current.

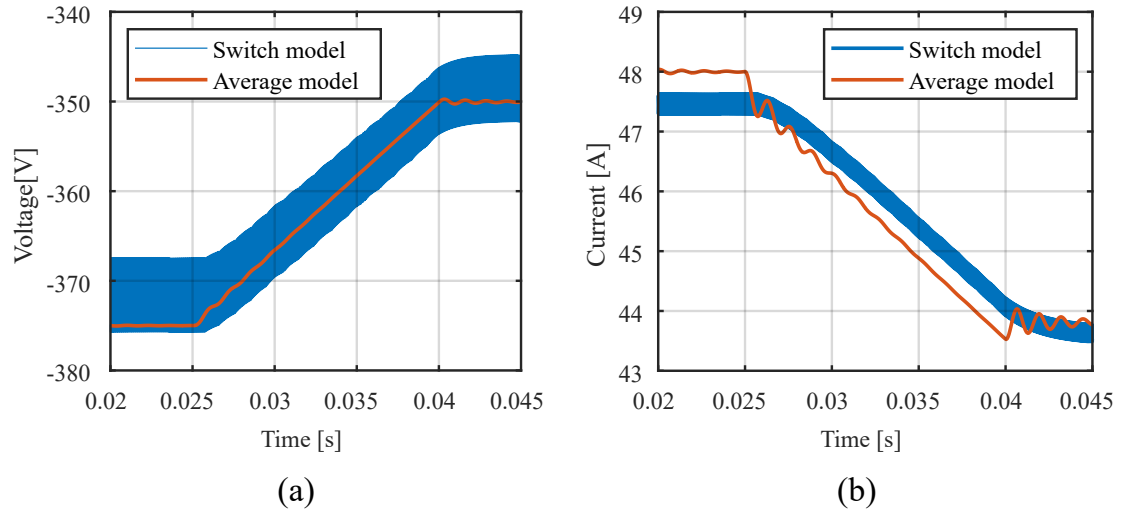


Figure 15. Switch and average two-port DC/DC converter ramp response comparison: (**a**) Output voltage, (**b**) HFAC link current.

To compare the computing time of both models, the time required to run each model is obtained via the Simulink profiler tool. Both simulations run for 50 ms with a step of 0.1 µs. The switched model requires 8.506 s, while the averaged model takes 3.365 s. The results show that the average model effectively reduces the computation time. Furthermore, the averaged model can operate with a larger time step without affecting its results, further decreasing the computational load.

The previous results have shown that the proposed average model provides the same steady-state values and dynamics as the state-space model. Furthermore, the comparison with the switched model demonstrates that the average model can replicate both the magnitude and the dynamics of the switched model. Thus, the proposed average model can be applied to studies where the converter currents and power transfers are analyzed, while the switching dynamics are neglected. One such case is the modeling of multiple converters in parallel in a DC microgrid. In such a case, the power transfer between converters and the implemented control are the main elements under study. Implementing such a system with the switched model requires high computational demand, and thus using the proposed average model alleviates the computational requirements while maintaining the main system dynamics.

3. Modeling of Three-Port DC/DC/DC Converters

In this section, the modeling of three-port HFAC link converters is developed. These converters have the same operating mechanisms (ZVS, energy transfer via HFAC link, resonance periods to adjust voltage of the HFAC link) as the previously shown two-port converters but have an additional port that allows the connection of either another source or load. The modeling for two cases will be developed: two sources, one load, and one source, two loads.

3.1. Two Sources, One Load

The methodology used in the previous section is applied to the three-port converter. The three-port converter considered has the topology shown in Figure 16. The two sources are represented by V_1 and V_2.

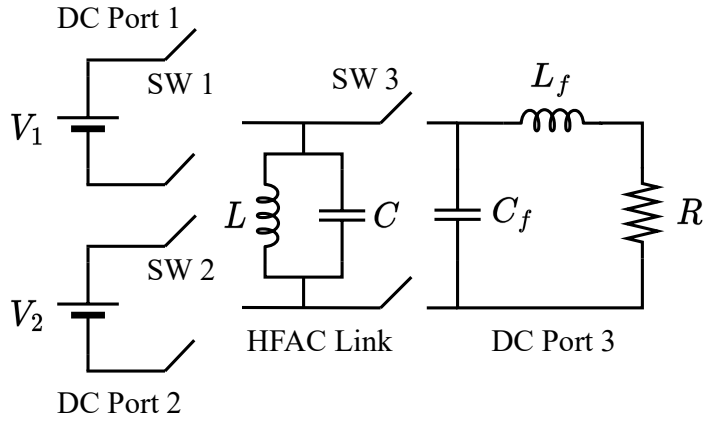


Figure 16. Three-port DC/DC/DC converter circuit diagram: two sources, one load.

As in the previous section, the general operation of the converter is explained via the voltage and current waveforms shown in Figure 17. First, the port with the highest voltage, V_1, will charge the link inductance. After a resonance period, the second port will charge the last part of the inductance with a voltage, V_2. Once the inductance is charged, the link will resonate to the third port voltage, V_{C_f}, and discharge the inductance. The process is then repeated with reversed polarity.

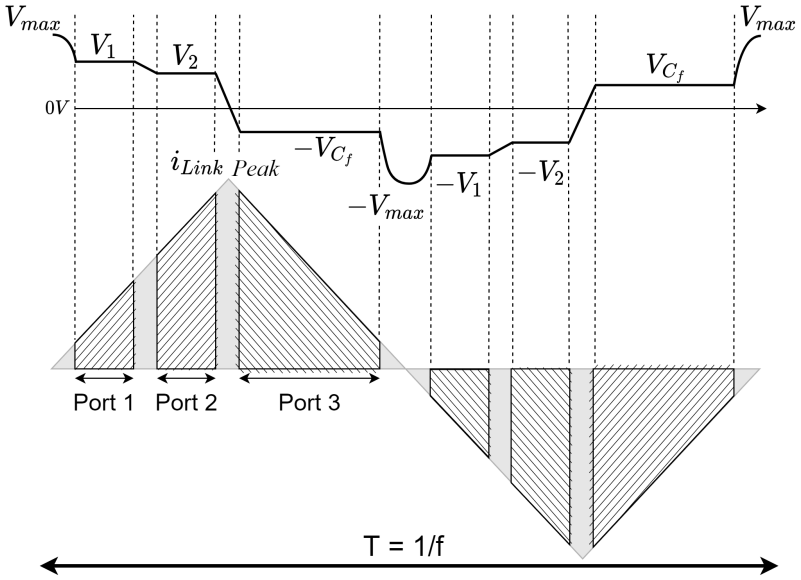


Figure 17. Three-port DC/DC/DC converter two sources, one load HFAC link voltage and current waveform ©2023 IEEE. Reproduced with copyright permission from [15].

The first step is to define the equations for each different state: when only SW1 is connected, when only SW2 is connected, and when only SW3 is connected. The state variables remain the same as in the two-port case. However, there is an additional input and an additional switch case, and thus a third duty cycle, d_3. The state equations for the connection of SW1, SW2, and SW3 are given in Equations (15), (16), and (17), respectively.

$$\begin{cases} L\frac{dI_L}{dt} = V_1 \\ L_f\frac{dI_{L_f}}{dt} = -I_{L_f}R + V_{C_f} \\ C_f\frac{dV_{C_f}}{dt} = -\frac{V_{C_f}}{R} \end{cases} \tag{15}$$

$$\begin{cases} L\frac{dI_L}{dt} = V_2 \\ L_f\frac{dI_{L_f}}{dt} = -I_{L_f}R + V_{C_f} \\ C_f\frac{dV_{C_f}}{dt} = -\frac{V_{C_f}}{R} \end{cases} \tag{16}$$

$$\begin{cases} L\frac{dI_L}{dt} = V_{C_f} \\ L_f\frac{dI_{L_f}}{dt} = -I_{L_f}R + V_{C_f} \\ C_f\frac{dV_{C_f}}{dt} = -I_L - \frac{V_{C_f}}{R} \end{cases} \tag{17}$$

With the equations in hand, it is possible to set up the state-space model as follows:

$$\dot{\bar{x}} = A\bar{x} + B\bar{u}, \tag{18}$$

where:

$$A = d_1A_1 + d_2A_2 + d_3A_3$$
$$B = d_1B_1 + d_2B_2 + d_3B_3$$
$$A_1 = A_2 = \begin{bmatrix} 0 & 0 & 0 \\ 0 & \frac{-R}{L_f} & \frac{1}{L_f} \\ 0 & 0 & -\frac{1}{C_fR} \end{bmatrix}$$
$$A_3 = \begin{bmatrix} 0 & 0 & \frac{1}{L} \\ 0 & \frac{-R}{L_f} & \frac{1}{L_f} \\ -\frac{1}{C_f} & 0 & -\frac{1}{C_fR} \end{bmatrix}$$
$$B_1 = \begin{bmatrix} \frac{1}{L} \\ 0 \\ 0 \end{bmatrix}, B_2 = \begin{bmatrix} 0 \\ \frac{1}{L} \\ 0 \end{bmatrix}, B_3 = \begin{bmatrix} 0 \\ 0 \\ 0 \end{bmatrix}$$

From the state-space system, the definition for the steady-state values of the state variables is found as:

$$\begin{cases} I_L = \frac{V_1d_1}{Rd_3^2} + \frac{V_2d_2}{Rd_3^2} \\ I_f = -\frac{V_1d_1}{Rd_3} - \frac{V_2d_2}{Rd_3} \\ V_{C_f} = \frac{-V_1d_1}{d_3} - \frac{-V_2d_2}{d_3} \end{cases} \tag{19}$$

3.1.1. Model Validation

To validate the system, the values of Table 3 are plugged into the state-space model. The results from the state-space model are then compared against the expected values. The peak value of the inductor current and the duty cycles are determined using the methodology developed in [12]. In [12], it is shown that the expression for the peak current in the HFAC

link can be found as shown in Equation (20), with $P_0 = 0$. Similarly, the frequency of the link based on the power and inductance can be found as shown in Equation (21).

$$I_{L,peak} = 2\sqrt{P_{in}} \sum_{i=0}^{n+m-1} \frac{\sqrt{\sum_{i=0}^{i} P_{i+1}} - \sqrt{\sum_{i=0}^{i} P_i}}{V_{i+1}} \tag{20}$$

$$f = \frac{P_{in}}{L I_{L,peak}^2} \tag{21}$$

Once the frequency is found, it is possible to calculate the duration of each charge or discharge period as:

$$t_{i+1} = \frac{L}{f} \frac{\sqrt{\sum_{i=0}^{i} P_{i+1}} - \sqrt{\sum_{i=0}^{i} P_i}}{V_{i+1}}, \; i = 0, 1, 2, \ldots, n-1 \tag{22}$$

The average inductance current, L, is calculated through the area of the waveform, as shown in Figure 17. The formula shown in Equation (23) represents the sum of the areas of two triangles and a trapezoid.

$$I_{Lavg} = \frac{1}{T}(0.5\, t_1\, I_1 + 0.5\, (I_1 + I_{Lpeak})\, t_2 + 0.5\, t_3\, I_{Lpeak}), \tag{23}$$

where I_1 represents the peak current attained by the first port. As in the two-port case, the duty cycle of each port can be calculated using the period duration, t_i, and the total period, T, as shown in Equation (24).

$$d_1 = \frac{t_1}{T};\; d_2 = \frac{t_2}{T};\; d_3 = \frac{t_3}{T} \tag{24}$$

The parameters presented in Table 3 are used to compare the results of the equations to those of the state-space system. The following duty cycles are obtained with the previous Equations: $d_1 = 0.2449$, $d_2 = 0.1136$, and $d_3 = 0.6414$. Table 4 shows the obtained results for both models for the inductor current, I_L, output current, I_{L_f}, and the output voltage, V_{C_f}.

Table 3. Three-port DC/DC/DC converter parameters with two sources, one load.

Parameter	Value
P_{max} (kW)	20
P_1 (kW)	7
P_2 (kW)	5
Link Frequency (kHz)	5
V_1 (V)	750
V_2 (V)	500
V_{C_f} (V)	375
Link inductance (mH)	0.156
Filter inductance (µH)	6.2
Filter capacitance (mF)	120

Table 4. Three-port converter state-space model output values comparison.

Parameter	Analytical Equations	State-Space Model
I_L (A)	51.333	49.890
I_{L_f} (A)	−32	−32
V_{C_f} (V)	−375	−375

It is seen that the result provided for I_L has a small deviation from the expected value. To further analyze the result, the output power, P_{out}, is calculated. The power given to the load can be obtained using the output current equation shown in Equation (19) as follows:

$$P_{out} = V_{C_f} \left(\frac{V_1 \, d_1}{R \, d_3} + \frac{V_2 \, d_2}{R \, d_3} \right). \tag{25}$$

In Equation (25), each fraction corresponds to the power of each port. If calculated using the previously shown parameters, the results obtained are $P_1 = 9.165$ kW and $P_2 = 2.835$ kW, which do not correspond to the expected $P_1 = 7$ kW and $P_2 = 5$ kW. The source of this error can be attributed to the fact that the state-space model does not consider the value of I_1 nor the trapezoid in the middle of the waveform. Thus, in order to obtain the correct values, a new set of duty cycles, ds, can be calculated. These are calculated by considering the average port current and average inductance current, I_{Lavg}, as follows:

$$d_1 s = \frac{I_{P1avg}}{I_{Lavg}}. \tag{26}$$

The new calculated duty cycles are shown in Table 5 along with the ones first calculated. If the calculations are performed again with the new duty cycles, ds, the proper power distribution is obtained with $P_1 = 7$ kW and $P_2 = 5$ kW. Furthermore, solving the state-space system provides the correct average inductor current while retaining the correct value for the other state variables, as shown in Table 6. Note that when using a PI controller, the controller will tend to the correct duty cycle, ds, as it operates based on the output values. Therefore, if a PI controller is implemented there is no iterative calculation of the duty cycle.

Table 5. Three-port DC/DC/DC converter calculated duty cycles.

Port	*d*	*ds*
P_1	0.2449	0.1818
P_2	0.1136	0.1948
P_3	0.6414	0.6234

Table 6. Three-port DC/DC/DC converter state-space model output values comparison with new duty cycles.

Parameter	Analytical Equations	State-Space Model
I_L (A)	51.333	51.333
I_{L_f} (A)	−32	−32
V_{C_f} (V)	−375	−375

As with the two-port converter, the transfer function for this converter can also be derived. The output voltage step response of the developed model is depicted in Figure 18. In this case, the output voltage step response is the sum of the response to two different steps. Indeed, one part of the response is linked to the step to the voltage, V_1, while the other is linked to the input, V_2. Figure 18 displays the individual contributions of each input voltage to the output voltage response. The cumulative effect of these responses results in the output voltage reaching a steady-state value of −375 V, which is the desired output voltage.

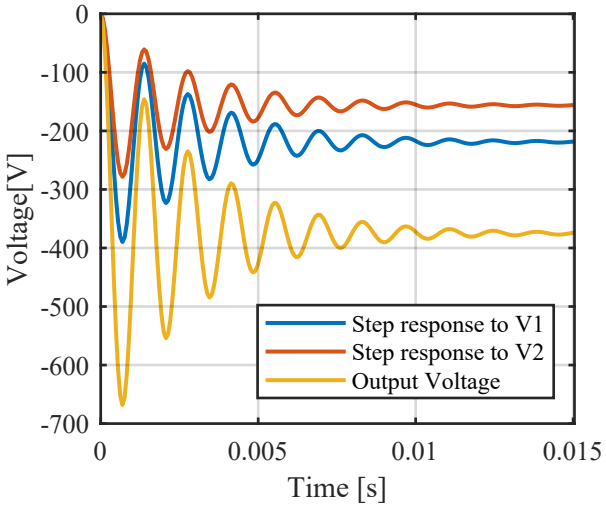


Figure 18. Three-port DC/DC/DC covnerter output voltage step response to inputs V_1 and V_2.

3.1.2. Average Model

Using the Variable-ratio transformer block, the three-port converter is implemented as shown in Figure 19. The two inputs are connected in series via the transformers. The two voltages resulting from the transformers with turn ratios d_1s and d_2s make one equivalent voltage that is applied to the inductance and then transformed by a ratio, d_3s. Notice that the case represented here corresponds to two sources feeding one load. For the case where one source feeds two loads, the circuit does not need to be modified. Applying a negative sign to the duty cycle of Port 1 or Port 2 is all that is required to change their behavior into that of a load. The proposed circuit is implemented here with the parameters described in Table 3 and the new duty cycles, ds, of Table 5.

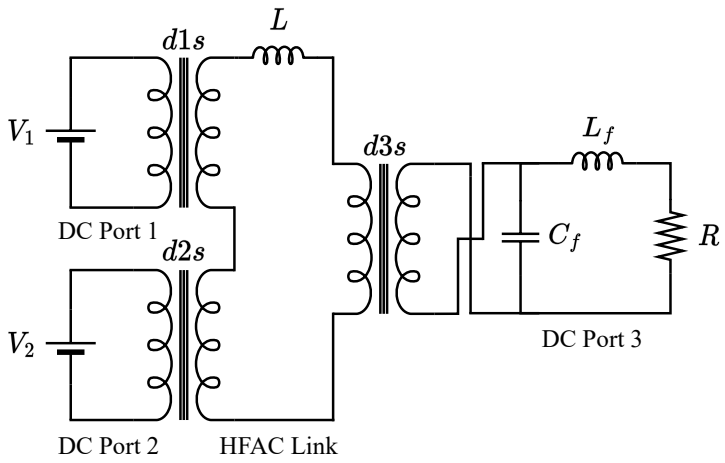


Figure 19. Average three-port DC/DC/DC converter implementation with two sources, one load.

As with the two-port case, three different signals of interest are shown. In Figure 20a, the output voltage is shown. It can be observed that the signal stabilizes to the expected value of -375 V. Afterwards, in Figure 20b,c, the average link current, I_L, and the output current, I_{Lf}, are displayed, respectively. It is seen that both signals also achieve the expected values.

Finally, the response of the Simulink model is compared to that of the transfer function. The response to a 5% drop in the input voltages will be tested. First, a voltage drop will be applied to V_1. After the system stabilizes, a second 5% voltage drop will be applied to V_2. Figure 21 shows the described sequence where the first voltage drop is applied at $t = 0.5$ s. Compared to the two-port case of Figure 11, it is seen that the voltage deviation is lower and the settling point is different in the three-port converter. This can be attributed to the

fact that the load is being fed by two different sources. Thus, a part of the supply remains undisturbed. At $t = 0.52$ s, the voltage drop on V_2 is applied. It is shown that, after this perturbation, the system stabilizes to a value close to -356.3 V, which is similar to the final value for the two-port converter.

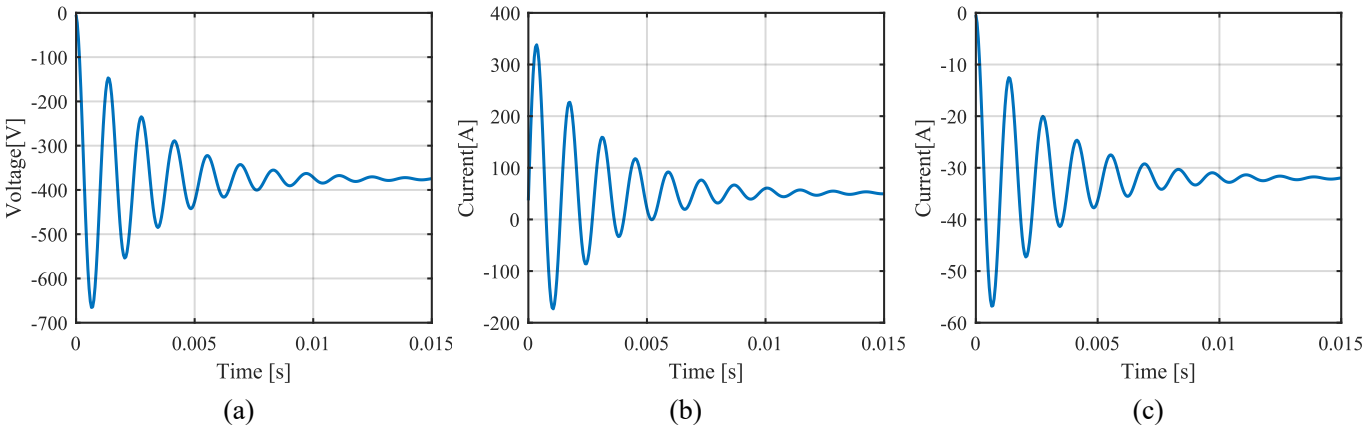


Figure 20. Three-port DC/DC/DC converter two sources, one load Simulink implementation: (**a**) Output voltage, V_{C_f}, (**b**) Link current, I_L, (**c**) Output inductance current, I_{Lf}.

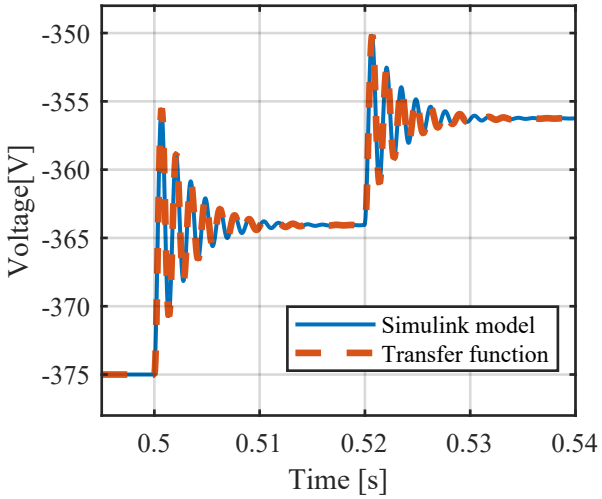


Figure 21. Three-port DC/DC/DC converter two sources, one load output voltage response to a 5% input voltage drop on both sources.

3.2. One Source, Two Loads

The scenario in which a single source supplies two different loads is considered. The simplified circuit of the converter in this scenario is shown in Figure 22. Here, the source is connected to Port 2, while the loads are connected to Port 1 and Port 3.

The operation and switching behaviors of the converter are illustrated in Figure 23. Initially, The HFAC link is connected to Port 2, which has a source with voltage V_2. This source charges the link inductance, increasing the current in the HFAC link linearly. Once the link is charged to the desired value, the HFAC link is disconnected. This is followed by a resonance period, during which the voltage is adjusted to match the voltage of the next port. Once the voltage of Port 3 is reached, the HFAC link is connected with opposite polarity and partially discharges the inductance to the load. After the initial discharge, the HFAC link disconnects, entering another resonance period to adjust its voltage to that of Port 1. After connecting to the final port, the remaining link current is discharged to the second load. A final resonance occurs, swinging the voltage up to the maximum value, V_{max}, before

returning to the input voltage, where the cycle recommences. once again, a second energy transfer is performed with opposite voltage polarity to enhance the system's efficiency.

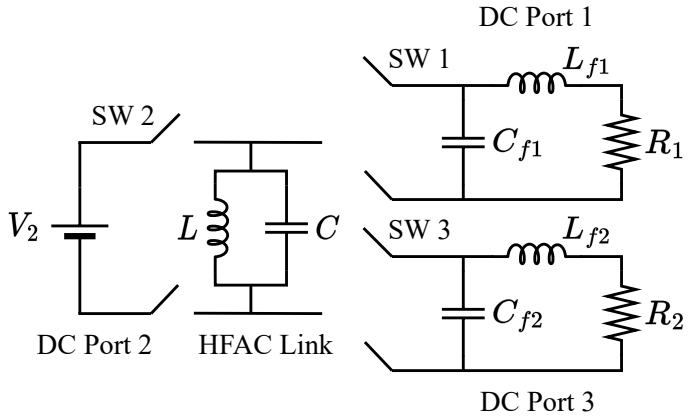


Figure 22. Simplified three-port DC/DC/DC converter circuit diagram: one source, two loads.

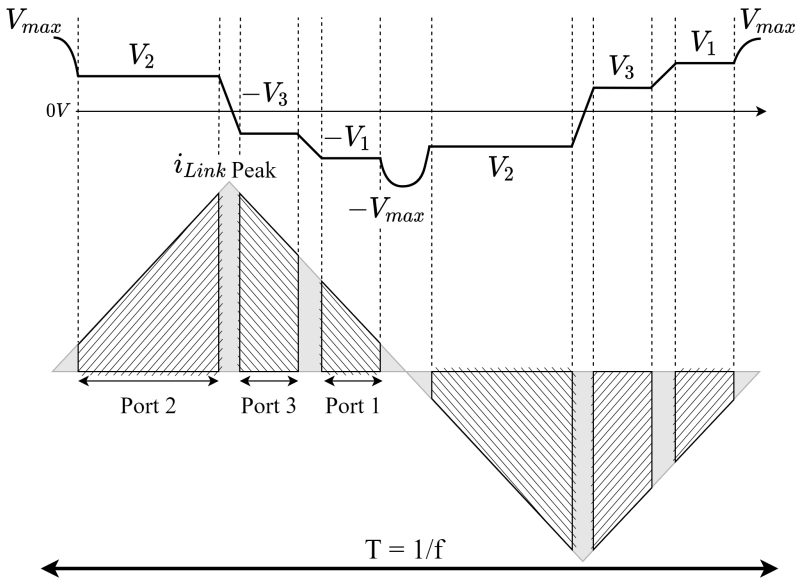


Figure 23. Three-port DC/DC/DC one source, two loads voltage and current waveform.

The circuit is analyzed considering five state variables: link-inductance current, I_L, output filter inductance currents, $I_{L_{f1}}$ and $I_{L_{f2}}$, and the output filter capacitor voltages, $V_{C_{f1}}$ and $V_{C_{f2}}$. Three different switch cases are considered. First, when SW2 is closed and the inductance, L, is charged, the system is described by the equations shown in (27). The second case, when SW1 is closed and the first load, R_1, is supplied, is described by (28). Finally, the equations for SW3 being closed, which corresponds to the discharge towards the second load, R_2, are given in (29).

$$\begin{cases} L\frac{dI_L}{dt} = V_2 \\ L_{f1}\frac{dI_{L_{f1}}}{dt} = V_{C_{f1}} - I_{L_{f1}}R_1 \\ C_{f1}\frac{dV_{C_{f1}}}{dt} = -\frac{V_{C_{f1}}}{R_1} \\ L_{f2}\frac{dI_{L_{f2}}}{dt} = V_{C_{f2}} - I_{L_{f2}}R_2 \\ C_{f2}\frac{dV_{C_{f2}}}{dt} = -\frac{V_{C_{f2}}}{R_2} \end{cases} \tag{27}$$

$$\begin{cases} L\frac{dI_L}{dt} = -V_3 \\ L_{f1}\frac{dI_{L_{f1}}}{dt} = V_{C_{f1}} - I_{L_{f1}}R_1 \\ C_{f1}\frac{dV_{C_{f1}}}{dt} = -I_L - \frac{V_{C_{f1}}}{R_1} \\ L_{f2}\frac{dI_{L_{f2}}}{dt} = V_{C_{f2}} - I_{L_{f2}}R_2 \\ C_{f2}\frac{dV_{C_{f2}}}{dt} = -\frac{V_{C_{f2}}}{R_2} \end{cases} \tag{28}$$

$$\begin{cases} L\frac{dI_L}{dt} = -V_1 \\ L_{f1}\frac{dI_{L_{f1}}}{dt} = V_{C_{f1}} - I_{L_{f1}}R_1 \\ C_{f1}\frac{dV_{C_{f1}}}{dt} = -\frac{V_{C_{f1}}}{R_1} \\ L_{f2}\frac{dI_{L_{f2}}}{dt} = V_{C_{f2}} - I_{L_{f2}}R_2 \\ C_{f2}\frac{dV_{C_{f2}}}{dt} = -I_L - \frac{V_{C_{f2}}}{R_2} \end{cases} \tag{29}$$

With the previous equations in hand, the state-space model can be defined using a state matrix, A, input matrix, B, and the state vector, x. The duration of the intervals during which SW2, SW1, or SW3 are closed is indicated by the duty cycles d_1, d_2, and d_3, respectively. Therefore, the state-space model is expressed as:

$$\dot{\bar{x}} = A\bar{x} + B\bar{u}, \tag{30}$$

where:

$$A = d_1A_1 + d_2A_2 + d_3A_3$$
$$B = d_1B_1 + d_2B_2 + d_3B_3$$
$$A_1 = \begin{bmatrix} 0 & 0 & 0 & 0 & 0 \\ 0 & \frac{-R_1}{L_{f1}} & \frac{1}{L_{f1}} & 0 & 0 \\ 0 & 0 & -\frac{1}{C_{f1}R_1} & 0 & 0 \\ 0 & 0 & 0 & \frac{-R_2}{L_{f2}} & \frac{1}{L_{f2}} \\ 0 & 0 & 0 & 0 & \frac{-1}{C_{f2}R_2} \end{bmatrix}$$
$$A_2 = \begin{bmatrix} 0 & 0 & \frac{1}{L} & 0 & 0 \\ 0 & \frac{-R_1}{L_{f1}} & \frac{1}{L_{f1}} & 0 & 0 \\ \frac{-1}{C_{f1}} & 0 & -\frac{1}{C_{f1}R_1} & 0 & 0 \\ 0 & 0 & 0 & \frac{-R_2}{L_{f2}} & \frac{1}{L_{f2}} \\ 0 & 0 & 0 & 0 & \frac{-1}{C_{f2}R_2} \end{bmatrix}$$
$$A_3 = \begin{bmatrix} 0 & 0 & 0 & 0 & \frac{1}{L} \\ 0 & \frac{-R_1}{L_{f1}} & \frac{1}{L_{f1}} & 0 & 0 \\ 0 & 0 & -\frac{1}{C_{f1}R_1} & 0 & 0 \\ 0 & 0 & 0 & \frac{-R_2}{L_{f2}} & \frac{1}{L_{f2}} \\ \frac{-1}{C_{f2}} & 0 & 0 & 0 & \frac{-1}{C_{f2}R_2} \end{bmatrix}$$
$$B_1 = \begin{bmatrix} \frac{1}{L} \\ 0 \\ 0 \\ 0 \\ 0 \end{bmatrix}, B_2 = B_3 = \begin{bmatrix} 0 \\ 0 \\ 0 \\ 0 \\ 0 \end{bmatrix}$$

From the state-space system, the expression for the steady-state values of the state variables can be found, as shown in (31). Moreover, by utilizing the state-transition matrix $\Phi = (sI - A)^{-1}$, the transfer functions for the state variables can be acquired through

the expression $H(s) = C\Phi B + D$. The resulting transfer functions are shown in (32). The average model for this case can be implemented, as shown in Figure 24.

$$\begin{cases} I_L = \frac{V_2\, d_1}{R_1\, d_2^2 + R_2\, d_3^2} \\ I_{f1} = -\frac{V_2\, d_1\, d_2}{R_1\, d_2^2 + R_2\, d_3^2} \\ V_{C_{f1}} = -\frac{R_1\, V_2\, d_1\, d_2}{R_1\, d_2^2 + R_2\, d_3^2} \\ I_{f2} = -\frac{V_2\, d_1\, d_3}{R_1\, d_2^2 + R_2\, d_3^2} \\ V_{C_{f2}} = -\frac{R_2\, V_2\, d_1\, d_3}{R_1\, d_2^2 + R_2\, d_3^2} \end{cases} \tag{31}$$

$$\begin{aligned} \frac{I_L}{V_2} &= \frac{d1s^2 + \frac{d_1}{L C_{f2} R_2} s - \frac{d_1}{L C_{f1} R_1} s + \frac{d1}{L C_{f1} C_{f2} R_1 R_2}}{s^3 + (\frac{1}{C_{f2} R_2} + \frac{1}{C_{f1} R_1}) s^2 + (\frac{1}{C_{f2} C_{f1} R_1 R_2} + \frac{d_2^2}{L C_{f1}} + \frac{d_3^2}{L C_{f2}}) s + \frac{d_2^2}{L C_{f2} C_{f1} R_2} + \frac{d_3^2}{L C_{f2} C_{f1} R_1}} \\ \frac{I_{L_{f1}}}{V_2} &= \frac{1}{L_{f1} s + R_1} \frac{-\frac{d_2\, d_1}{L C_f} s - \frac{d_2\, d_1}{L C_{f2} C_{f1} R_2}}{s^3 + (\frac{1}{C_{f2} R_2} + \frac{1}{C_{f1} R_1}) s^2 + (\frac{1}{C_{f2} C_{f1} R_1 R_2} + \frac{d_2^2}{L C_{f1}} + \frac{d_3^2}{L C_{f2}}) s + \frac{d_2^2}{L C_{f2} C_{f1} R_2} + \frac{d_3^2}{L C_{f2} C_{f1} R_1}} \\ \frac{V_{C_{f1}}}{V_2} &= \frac{-\frac{d_2\, d_1}{L C_f} s - \frac{d_2\, d_1}{L C_{f2} C_{f1} R_2}}{s^3 + (\frac{1}{C_{f2} R_2} + \frac{1}{C_{f1} R_1}) s^2 + (\frac{1}{C_{f2} C_{f1} R_1 R_2} + \frac{d_2^2}{L C_{f1}} + \frac{d_3^2}{L C_{f2}}) s + \frac{d_2^2}{L C_{f2} C_{f1} R_2} + \frac{d_3^2}{L C_{f2} C_{f1} R_1}} \\ \frac{I_{L_{f2}}}{V_2} &= \frac{1}{L_{f2} s + R_2} \frac{-\frac{d_2\, d_1}{L C_f} s - \frac{d_2\, d_1}{L C_{f2} C_{f1} R_2}}{s^3 + (\frac{1}{C_{f2} R_2} + \frac{1}{C_{f1} R_1}) s^2 + (\frac{1}{C_{f2} C_{f1} R_1 R_2} + \frac{d_2^2}{L C_{f1}} + \frac{d_3^2}{L C_{f2}}) s + \frac{d_2^2}{L C_{f2} C_{f1} R_2} + \frac{d_3^2}{L C_{f2} C_{f1} R_1}} \\ \frac{V_{C_{f2}}}{V_2} &= \frac{-\frac{d_3\, d_1}{L C_{f2}} s - \frac{d_3\, d_1}{L C_{f2} C_{f1} R_1}}{s^3 + (\frac{1}{C_{f2} R_2} + \frac{1}{C_{f1} R_1}) s^2 + (\frac{1}{C_{f2} C_{f1} R_1 R_2} + \frac{d_2^2}{L C_{f1}} + \frac{d_3^2}{L C_{f2}}) s + \frac{d_2^2}{L C_{f2} C_{f1} R_2} + \frac{d_3^2}{L C_{f2} C_{f1} R_1}} \end{aligned} \tag{32}$$

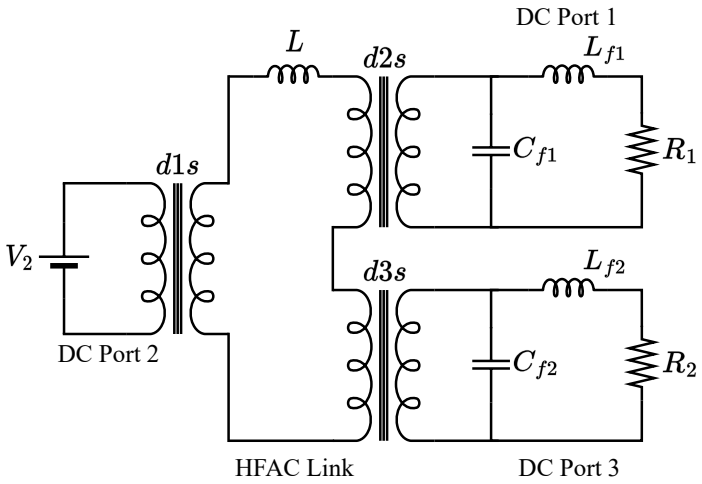


Figure 24. Average three-port DC/DC/DC converter implementation with one, source two loads.

Three-Port DC/DC/DC Converter One Source, Two Loads Pole Zero Analysis

A converter with the parameters shown in Table 7 is considered. The eigenvalues of matrix A that describe the dynamics of the converter are shown in Table 8. It is shown that all the eigenvalues are located on the left-hand side of the plane, indicating that the system is stable. The first two poles have high magnitude values that are defined by R/L_f. Specifically, these poles correspond to the initial fraction encountered in the transfer functions of $I_{L_{f1}}$ and $I_{L_{f2}}$ in Equation (32).

Table 7. Three-port DC/DC/DC 50 kW converter parameters with one source, two loads.

Parameter	Value
P_{max} (kW)	50
Link Frequency (kHz)	5
Link inductance (µH)	62.5
V_1 (V)	750
V_2 (V)	500
V_3 (V)	375
L_{f1} (µH)	2.31
L_{f2} (µH)	16.65
C_f (mF)	17.78
C_{f2} (mF)	4.44
R_1 (Ω)	11.25
R_2 (Ω)	28.125

Table 8. Three-port DC/DC/DC 50 kW converter with one source, two loads eigenvalues.

Parameter	Value
-4.8655×10^{6}	0
-1.6888×10^{6}	0
-5.8427	0
-3.5786	477.31
-3.5786	-477.31

The predominant dynamics of the systems are governed by the lowest three eigenvalues listed in Table 8. The transfer functions reveal a pronounced coupling among distinct outputs. This coupling emerges due to the interplay between the loads, filters of individual ports, and the three duty cycles. This can be illustrated by studying the behavior of the poles of the transfer function of $V_{C_{f1}}$. Figure 25 depicts the pole displacement resulting from incremental increases of 5 Ω in each of the load resistances. It is seen that changing the load resistance, R_2, of the other output port induces a shift in the poles of $V_{C_{f1}}$. Notably, the poles remain on the left-hand side of the plane, indicating that the system remains stable.

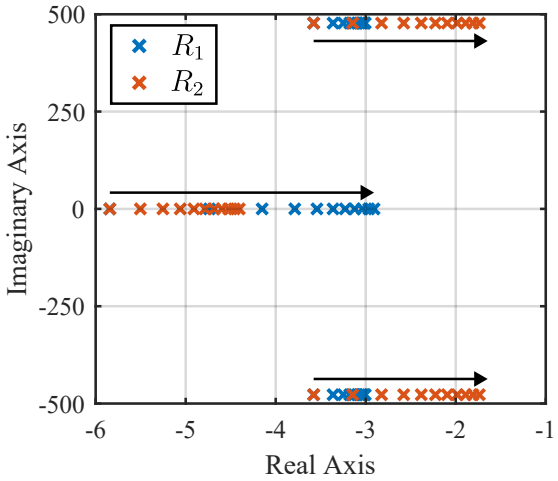


Figure 25. Impact of load resistors size on $V_{C_{f1}}$ response. Arrow indicates the direction of movement of the poles as the value of the resistances increase.

A similar test is performed with the filter capacitors. Figure 26 shows the displacements of the poles for the transfer function of $V_{C_{f1}}$ as the values of the filter capacitors are individually increased by 5 µF. Similar to the case of resistances, it is demonstrated that altering the filter capacitance of either port impacts the behavior of $V_{C_{f1}}$, highlighting the

presence of coupling within the system. As in the previous case, the poles remain on the left-hand side of the plane, thus ensuring the stability of the system.

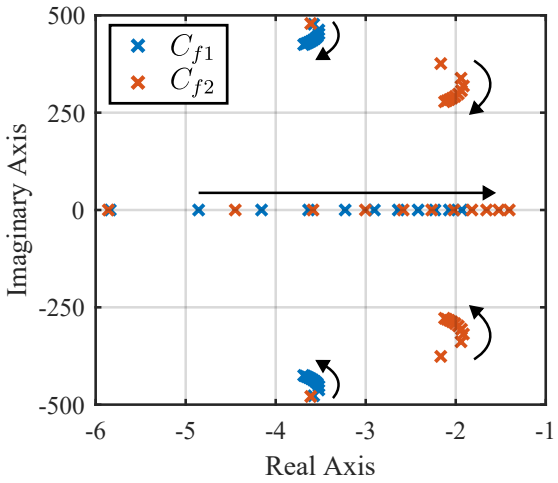


Figure 26. Impact of filter capacitors size on $V_{C_{f1}}$ response. Arrow indicates the direction of movement of the poles as the value of the capacitors increase.

4. Control of Three-Port DC/DC/DC Converters

As shown through the state-space model, the average model is controlled through the use of three duty cycles. In this section, the implemented control for each port through the use of these duty cycles is detailed. Different combinations of loads and sources are considered to this effect.

4.1. Control with Batteries

The converters will be used within the context of a DC microgrid. It is considered that one port will manage the voltage of the DC distribution bus. Therefore, the ports are assumed to be connected to three distinct elements: a battery acting as a source, a resistive load, and the DC microgrid bus. The port connected to the DC microgrid bus is controlled through droop control. Droop control consists of reducing or increasing the reference output voltage of the converter proportionally to the output current. This adjustment is achieved using a virtual resistance known as the droop resistance, R_d. By selecting the appropriate value of R_d for each converter, proportional load distribution among them can be ensured. However, the accuracy of load sharing can be reduced due to line resistances and their associated voltage drops [19]. The implementation of the droop control is as follows:

$$V_{DC} = V_{DC}^{*} - R_d\, I_o, \tag{33}$$

where V_{DC}^{*} is the nominal DC voltage and V_{DC} is the resulting new reference voltage. The measured output current, I_o, is multiplied by the virtual resistance, R_d. The resulting voltage is then subtracted from the nominal voltage, V_{DC}^{*}. The droop parameter can be calculated as shown in (34), where the allowed voltage deviation, Δ_V, is divided by the converter maximum output current, i_{max} [20].

$$R_d = \frac{\Delta_V}{i_{max}} \tag{34}$$

The port connected to the resistive load is controlled as a grid-forming port. In other words, it maintains its output voltage at the designated reference nominal voltage. Figure 27 shows the implementation of these two controllers. The normalized error is input to a Proportional-Integral (PI) controller, which generates the duty cycle for each port. Although the converter is controlled via three duty cycles, only two controllers are needed. Indeed, the third duty cycle is found through the relationship $1 = d_{Grid} + d_{Load} + d_{Battery}$.

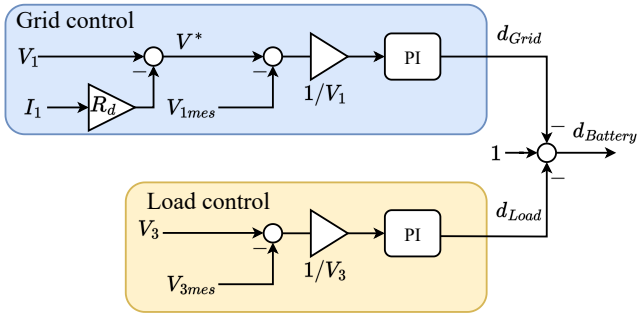


Figure 27. Control scheme for battery-fed three-port DC/DC/DC converters connected to the DC microgrid and a load.

4.2. Control with PVs

A similar controller is applied for converters that have PVs connected to them. The duty cycle for the PV panel port is determined directly by the Maximum Power Point Tracking (MPPT) algorithm, which seeks to maximize the power produced by the PV panels. Figure 28 shows the implemented controller for a converter connected to both PVs and a battery. Interaction with the grid is governed by the previously discussed droop control, while the PV port is managed using the MPPT algorithm. The battery maintains power balance between the other two ports by either absorbing or supplying the required power.

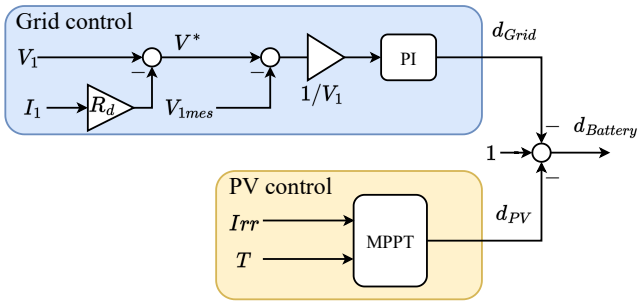


Figure 28. Control scheme for battery and PV-fed three-port DC/DC/DC converters connected to the DC microgrid.

Figure 29 illustrates the control strategy when a load is connected in place of a battery. The load port is controlled as a grid-forming port to ensure proper voltage regulation for the load. In this case, the DC microgrid is responsible for maintaining the power balance between the two other ports. Therefore, any surplus power will be injected into the DC microgrid, while any deficit in power will be supplied by the DC microgrid.

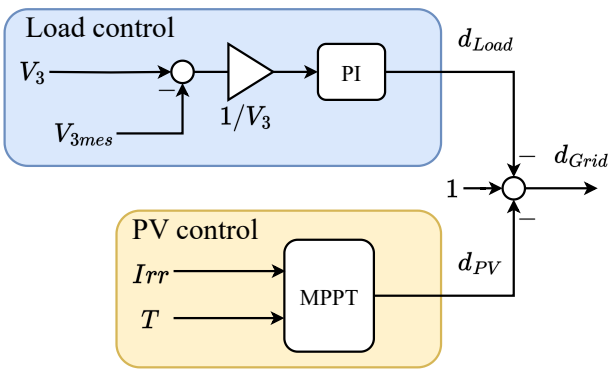


Figure 29. Control scheme for PV-fed three-port DC/DC/DC converters connected to the DC microgrid and a load.

5. Three-Port DC/DC/DC Converter DC Microgrid Implementation

To assess the performance of the proposed model, the DC microgrid shown in Figure 30 is implemented in Matlab/Simulink. This DC microgrid comprises four parallel-operating three-port converters, connected by lines of varying lengths. The ports of the converters shown in Figure 30 are equipped with PVs, batteries, loads, or a connection to the DC microgrid, as elaborated in Table 9. The averaged model of each converter is implemented as was shown in Section 3 in Figure 24. The utilized PV and battery models are the pre-existing ones within Simscape in Matlab/Simulink; 50 kW DC/DC/DC converters are used, which have the same parameters that were shown in Table 7. Each DC microgrid connected port has a voltage $V_1 = 750$ V and a filter with parameters L_{f2} and C_{f2}. The load ports have a voltage $V_3 = 375$ V and a filter with parameters L_{f1} and C_{f1}. The transmission lines used have a resistance of 0.194 Ω/km and an inductance of 1 mH/km.

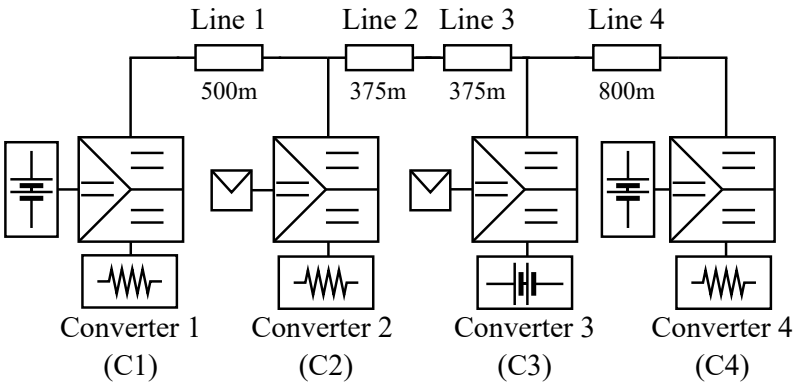


Figure 30. Implemented DC microgrid in Matlab/Simulink.

Table 9. Three-port DC/DC/DC converter port configuration.

Converter	Microgrid	Battery	PVs	Load
1	✓	✓		✓
2	✓		✓	✓
3	✓	✓	✓	
4	✓	✓		✓

Within the implemented DC microgrid, an initial load of 20 kW is positioned between Line 2 and Line 3. This load draws power from the DC microgrid ports of different converters. Converters 1 and 4 both have a 12.5 kW load, while Converter 3 has a 16 kW load. Two different events occur in the grid. At $t = 3$ s, the load of Converter 1 is increased to 18.75 kW, and at $t = 5$ s a second load of 14 kW is connected in the DC microgrid between Line 1 and Line 2. Figure 31a,b show, respectively, the evolution of the load voltages and the power supplied to each load during these events. It is seen that the nominal voltage value is reached. The events in the system cause perturbations in this voltage. As previously demonstrated, the converter ports are highly coupled, and adjustments in the duty cycle of one port will impact others correspondingly. This explains the origins of the perturbations seen. However, the perturbations are minimal as the voltage deviation stays below 0.01 p.u. It is seen that power is provided correctly to the loads, and the output power follows the expected reference.

The voltage of each port connected to the DC microgrid is shown in Figure 32a. As described in the previous section, the voltage of the DC microgrid is regulated by Converters 1, 3, and 4 using droop control. Thus, each converter will deviate from the nominal voltage proportionally to the power supplied. This is shown after $t = 5$ s, where the increase in power demand causes the voltage to deviate further from the nominal value. It is seen that the voltage is properly regulated, with the voltage deviations barely exceeding 0.95 p.u.

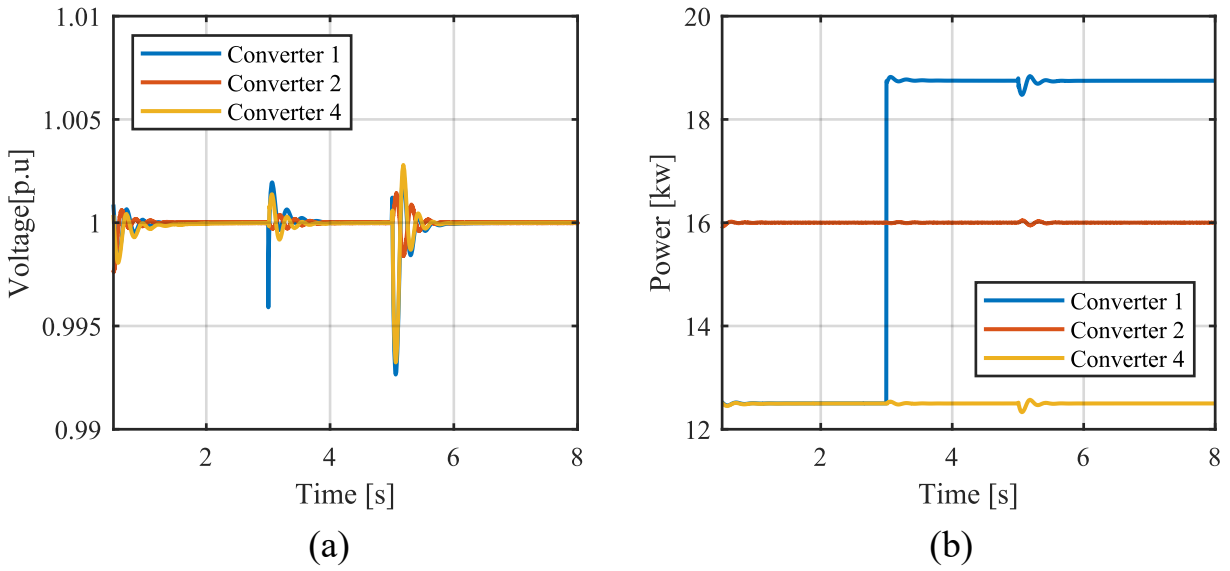


Figure 31. Three-port DC/DC/DC converters load-port output regulation: (**a**) Voltage, (**b**) Power supplied.

The power supplied to the DC microgrid by each converter is shown in Figure 32b. Due to its control strategy, Converter 2 does not directly regulate the DC voltage; rather, it injects any excess power generated by its PV panels. This explains the constant power injection exhibited by Converter 3 throughout the simulation. It is seen that Converters 1, 3, and 4 adapt their power injection to maintain the grid voltage. Although the same droop resistance is used in all three converters, the power injected by each one differs. This is due to the line impedance, which affects power distribution. When only one load is connected to the DC microgrid bus, it is Converter 3 that provides the most power, as it is the closest converter to the load. Converter 4 has a distance of 1175 m to the load and thus provides a lower amount of power. Upon connecting the second load, Converter 1 exhibits the most notable increase in its power output. This is due to the second load being the closest to Converter 1.

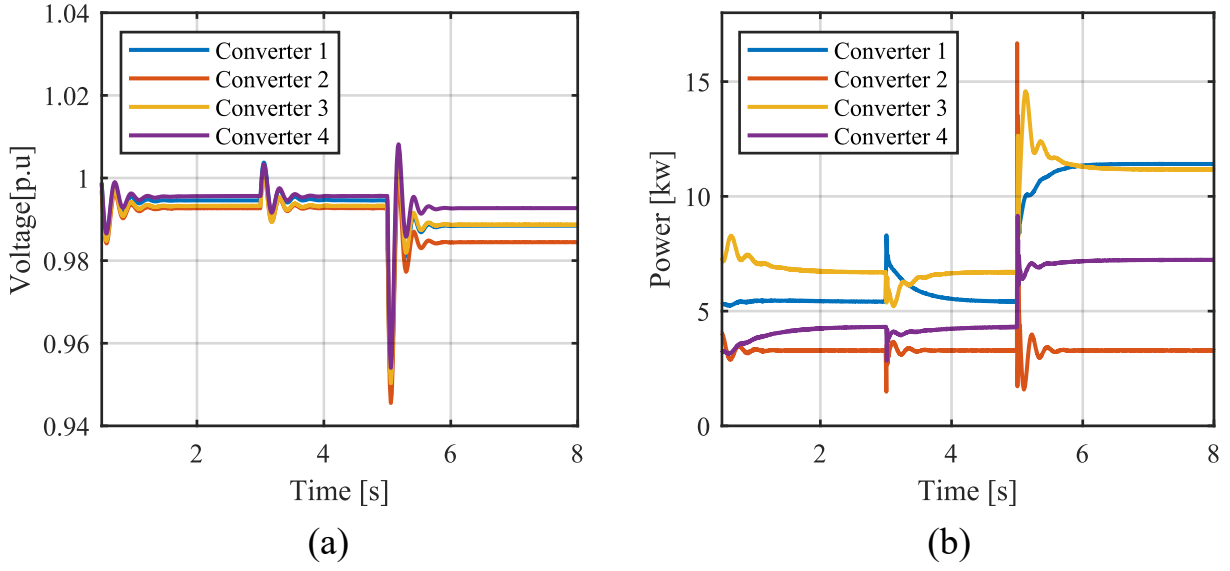


Figure 32. Three-port DC/DC/DC converters DC microgrid port output regulation: (**a**) Voltage, (**b**) Power supplied.

The power of each port of Converter 3 is shown in Figure 33. It is seen that the power output of the PV panels is kept constant through the MPPT control. Although the PVs generate more than 15 kW, this power is not directly injected into the DC microgrid. Instead, a portion of this output is injected in line with the load sharing achieved via droop control. It is shown that the surplus power is absorbed by the battery. Should the PV production decrease, the battery would discharge to maintain grid voltage and sustain load sharing.

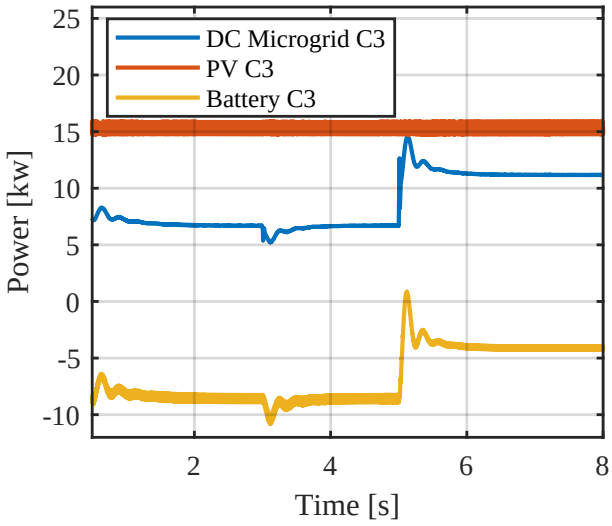


Figure 33. Power transfer in each port of Converter 3.

6. Conclusions

As the adoption of renewable energy sources continues to grow, there is an increasing need for converters in energy sources and storage systems. This demand is further driven by the rise in electric vehicles and other loads. Three-port converters utilizing a high-frequency AC link have emerged as a promising solution in this context. In this research, the advantages of high-frequency AC link converters and three-port converters were introduced. The operational principle of the converter was illustrated. An averaged model was specifically developed for this type of converter. A state-space model was formulated for the proposed converter. From the state-space model, the corresponding average value equations were obtained. The influence of the converter parameters on the placement of the system's poles was also considered. The principles were initially demonstrated using two-port converters and subsequently extended to three-port converters. It was highlighted that, due to the averaged nature of the model presented, the initially calculated duty cycles provide inaccurate power distribution. Thus, duty cycles taking into account the averaged model have to be used. The performance of the proposed model was validated through Simulink simulations, showcasing its ability to capture the essential characteristics of the system while significantly reducing computational complexity. Three control schemes were proposed for the converter according to the elements connected to each port. To validate the proposed model and control scheme, a DC microgrid with four three-port DC/DC/DC converters was simulated. The results showed proper voltage regulation for the loads and the DC microgrid bus. The results also demonstrated that the different control loops successfully achieved their different objectives.

In future work, the control of the converter will be further improved through cascade PI controllers, where a current control loop will be included. Furthermore, the addition of decoupling and feed-forward terms will be analyzed. Additionally, a comparison with experimental data/results could be performed.

Author Contributions: Conceptualization, E.V.M. and E.D.J.; methodology, E.V.M. and E.D.J.; validation, E.V.M. and E.D.J.; investigation, E.V.M. and E.D.J.; writing—original draft preparation, E.V.M.; writing—review and editing, E.V.M. and E.D.J. All authors have read and agreed to the published version of the manuscript.

Funding: This work was done in the context of the project MIRaCCLE (Micro-réseau Industriel avec Raccordement en Courant Continu et Luminaires Extérieurs), and supported by the government of the Région Wallonne of Belgium.

Data Availability Statement: All data are contained within the article.

Conflicts of Interest: The authors declare no conflicts of interest.

Abbreviations

The following abbreviations and symbols are used in this manuscript:

EV	Electric Vehicles
HFAC	High-Frequency AC
MPPT	Maximum Power Point Tracking
PI	Proportional Integral
PV	Photovoltaic
QSW	Quasi-Square Wave
ZVS	Zero Voltage Switching
A	State matrix
A_i	State matrix during duty cycle d_i
B	Input matrix
B_i	Input matrix during duty cycle d_i
C	HFAC link capacitor
C_f	Output filter capacitor
d_i	Duty cycle
ds	Modified duty cycle for three-port average converter
I_1	Peak current for first port in a three-port DC/DC/DC converter with two sources
I_L	HFAC link inductor current
I_{Lavg}	Average HFAC link-inductance current
I_{Lpeak}	Peak current of HFAC link inductance
I_{L_f}	Output filter inductance current
i_C	HFAC link capacitor current
i_{Link}	HFAC link current
i_{max}	Converter maximum output current
L	HFAC link inductance
L_f	Output filter inductance
P_{in}	Total input power
P_{out}	Total output power
P_i	Power for period t_i
R	Load resistance in a two-port DC/DC converter
R_d	Droop resistance
R_i	Load resistance i in a three-port DC/DC/DC converter with two loads
t_i	Charge or discharge period
T	Power transfer period
V_{C_f}	Output filter capacitor voltage
V_{DC}	Measured DC voltage
V^*_{DC}	Nominal DC bus voltage
V_{Link}	HFAC link voltage
V_{in}	Input voltage for a two-port DC/DC converter
V_{max}	HFAC link maximum voltage reached
V_i	Port i voltage for a three-port DC/DC/DC converter
x	State vector
Δ_v	Allowed voltage deviation
Φ	State-transition matrix

References

1. Zhang, N.; Sutanto, D.; Muttaqi, K.M. A review of topologies of three-port DC–DC converters for the integration of renewable energy and energy storage system. *Renew. Sustain. Energy Rev.* **2016**, *56*, 388–401. [CrossRef]
2. Vorperian, V. Quasi-square-wave converters: Topologies and analysis. *IEEE Trans. Power Electron.* **1988**, *3*, 183–191. [CrossRef]
3. Sood, P.; Lipo, T.; Hansen, I. A versatile power converter for high frequency link systems. In Proceedings of the 1987 IEEE Applied Power Electronics conference and Exposition, San Diego, CA, USA, 2–6 March 1987; pp. 249–256. [CrossRef]
4. Sood, P.; Lipo, T. Power conversion distribution system using a high-frequency AC link. *IEEE Trans. Ind. Appl.* **1988**, *24*, 288–300. [CrossRef]
5. Alexander, W.C. Universal Power Converter. U.S. Patent 7,778,045 B2, 17 August 2010.
6. Balakrishnan, A.; Toliyat, H.A.; Alexander, W.C. Soft switched ac link buck boost converter. In Proceedings of the 2008 Twenty-Third Annual IEEE Applied Power Electronics Conference and Exposition, Austin, TX, USA, 24–28 February 2008; pp. 1334–1339. [CrossRef]
7. Toliyat, H.A.; Balakrishnan, A.; Amirabadi, M.; Alexander, W. Soft switched ac-link AC/AC and AC/DC buck-boost converter. In Proceedings of the 2008 IEEE Power Electronics Specialists Conference, Rhodes, Greece, 15–19 June 2008; pp. 4168–4176. [CrossRef]
8. Amirabadi, M.; Balakrishnan, A.; Toliyat, H.A.; Alexander, W. Soft switched ac-link direct-connect photovoltaic inverter. In Proceedings of the 2008 IEEE International Conference on Sustainable Energy Technologies, Singapore, 24–27 November 2008; pp. 116–120. [CrossRef]
9. Amirabadi, M.; Balakrishnan, A.; Toliyat, H.A.; Alexander, W.C. High-Frequency AC-Link PV Inverter. *IEEE Trans. Ind. Electron.* **2014**, *61*, 281–291. [CrossRef]
10. Sadeghi, J.; Choolabi, E.F.; Zare, M.H. A new topology of unidirectional multistring PV inverter with high frequency AC-Link. In Proceedings of the 2016 24th Iranian Conference on Electrical Engineering (ICEE), Shiraz, Iran, 10–12 May 2016; pp. 1254–1259. [CrossRef]
11. Amirabadi, M.; Toliyat, H.A.; Alexander, W.C. A Multiport AC Link PV Inverter with Reduced Size and Weight for Stand-Alone Application. *IEEE Trans. Ind. Appl.* **2013**, *49*, 2217–2228. [CrossRef]
12. Alfares, A.; Mozaffari Niapour, S.A.K.H.; Amirabadi, M. High frequency AC microgrid based on a highly reliable single-stage converter. In Proceedings of the 2015 IEEE Energy Conversion Congress and Exposition (ECCE), Montreal, QC, Canada, 20–24 September 2015; pp. 2361–2367. [CrossRef]
13. Dosquet, R.; Rixhon, D.; Bleus, P. Future local intelligent transactional energy node for EV charging and mobility hub. In Proceedings of the CIRED Porto Workshop 2022: E-Mobility and Power Distribution Systems, Porto, Portugal, 2–3 June 2022; Volume 2022, pp. 965–969. [CrossRef]
14. Amirabadi, M.; Baek, J.; Toliyat, H.A.; Alexander, W.C. Soft-Switching AC-Link Three-Phase AC–AC Buck–Boost Converter. *IEEE Trans. Ind. Electron.* **2015**, *62*, 3–14. [CrossRef]
15. Allard, J.; Mayen, E.V.; De Jaeger, E. Resonance Model Comparison for High-Frequency AC Link Three-port Converter. In Proceedings of the 2023 IEEE International Conference on Environment and Electrical Engineering and 2023 IEEE Industrial and Commercial Power Systems Europe (EEEIC/I&CPS Europe), Madrid, Spain, 6–9 June 2023; pp. 1–6. [CrossRef]
16. Cuk, S. *Modeling, Analysis, and Design of Switching Converters*; California Institute of Technology: Pasadena, CA, USA, 1977.
17. Erickson, R.W.; Maksimovic, D. *Fundamentals of Power Electronics*; Springer: Cham, Switzerland, 2020.
18. The MathWorks Inc. Discrete Variable-Ratio Two-Winding Ideal Transformer, Natick, Massachusetts, USA, 2024. Available online: https://www.mathworks.com/help/sps/powersys/ref/variableratiotransformer.html (accessed on 13 May 2024).
19. Lu, X.; Guerrero, J.M.; Sun, K.; Vasquez, J.C. An Improved Droop Control Method for DC Microgrids Based on Low Bandwidth Communication with DC Bus Voltage Restoration and Enhanced Current Sharing Accuracy. *IEEE Trans. Power Electron.* **2014**, *29*, 1800–1812. [CrossRef]
20. Guerrero, J.M.; Vasquez, J.C.; Matas, J.; De Vicuña, L.G.; Castilla, M. Hierarchical control of droop-controlled AC and DC microgrids—A general approach toward standardization. *IEEE Trans. Ind. Electron.* **2010**, *58*, 158–172. [CrossRef]

Disclaimer/Publisher's Note: The statements, opinions and data contained in all publications are solely those of the individual author(s) and contributor(s) and not of MDPI and/or the editor(s). MDPI and/or the editor(s) disclaim responsibility for any injury to people or property resulting from any ideas, methods, instructions or products referred to in the content.